Title

RoMI: Robotic-microfluidic interface for biomedical analyses

Author

Zhou, Chuqing

Publication Date

2021

RoMI: Robotic-microfluidic interface for biomedical analyses

By

CHUQING ZHOU

DISSERTATION

Submitted in partial satisfaction of the requirements for the degree of

DOCTOR OF PHILOSOPHY

in

Chemical Engineering

in the

OFFICE OF GRADUATE STUDIES

of the

UNIVERSITY OF CALIFORNIA

DAVIS

Approved:

Cheemeng Tan, Chair

Gang Sun

Tingrui Pan

Committee in Charge

2021

Acknowledgement

Pursuing a doctorate has been a challenging but rewarding adventure, full of hardships and successes I have never experienced before. By overcoming difficulties over and over again, I have developed a calm mind and a heart that is full of love for what I do. Although the adventure is coming to an end, I will always remember those who encouraged and supported me on it.

To my major advisor, Professor Tingrui Pan, I was fortunate to become his student just as my interest in biomedical device research took shape. The first lesson he taught me was not to work behind closed doors. From talking with experts from different backgrounds in biotechnology fields, learning about the latest medical devices and related technologies, and by reaching out to physicians and entrepreneurs who understand real world needs, my horizons have been expanded, and the research direction I should devote my efforts to is clear. Dr. Pan guided me solve the many problems I faced during my research, by breaking down my goals, finding the core of a problem, brainstorming solutions, executing, and verifying. To use a Chinese proverb, Dr. Pan has not given me a fish, he has taught me how to fish. I am very grateful to him, and will follow his example as I dedicate myself to my future career.

To my co-advisor, Professor Cheemeng Tan – the perfect model of focus, enthusiasm, and thoughtfulness at work. Dr. Tan always inspired me, provided me with constructive suggestions and strengthened my logical thinking. I learned a lot of valuable professional skills under his guidance, from writing proposals, editing manuscripts and giving speeches, to conducting peer reviews and giving feedback and comments. Whether it is about the details of an experiment or advice for my future career, Dr. Tan has always made time to talk with me. His insights are

unfailingly honest and constructive. Without his support, this dissertation work would not have been possible.

I would like to give thanks to my dissertation committee, Professor Gang Sun, as well as committee members for my qualifying exam - Professor Jiandi Wan, Professor Harishankar Manikantan, Professor Erkin Seker and Professor Randy Carney. Thank you for your insightful comments and feedback on my qualifying exam and dissertation.

I would also like to thank major collaborators on my dissertation projects: Dr. Jingjing Wang, Dr. Zecong Fang and Xiyan Mai for advice and assistance on the design and fabrication of microfluidic devices; Dr. Ka Deng and Dr. Shiqiao Li for their instructions for RoMI system integration; Conary Meyer, Dr. Ji Young Shim, Cunyi Zhao and Shiva Emami for their insights and discussions on the biological applications of RoMI. My appreciation also goes to Professor Bruce D. Hammock and Professor Ameer Taha for their supports and inspirations.

Besides my collaborators, I also would like to thank my current and former lab mates in the MiNI lab: Dr. Zhichao Zhang, Yaojun Guo, Yi Ding, Dr. Hongcheng Wang; and in the Tan lab: Dr. Fan Wu, Dr. Daniel Lewis, Luis Eduardo Contreras Llano, Dr. Ting Gong, Dasha Aleksandra Iserlis, Hamad Abdullah Linjawi and Matthew Wong. I also want to thank all the great staff and professors in the Department of Chemical Engineering.

Finally, I would like to express my gratitude to my family and friends. Thanks to my parents, who cultivated my optimism and bravery, and who have always been there to support me. And thanks to my grandparents, who taught me to treat others with enthusiasm, sincerity, and tolerance. Without the benefit of their life experience, I could never have become who I am today.

This work was supported by the NIEHS UC Davis Superfund Project (5P42ES004699-30), National Institutes of Biomedical Imaging and Bioengineering (NIH-NIBIB) under award 1R21EB025938, NIH (5R21EB025938), and USDA-NIFA Grant (Grant No. 2018-67017-28116/Project Accession No. 1015597).

Abstract

In the past decades, a variety of accurate and reliable analytical technologies have been developed for the quantitative measurements of target analytes (e.g., proteins, metabolites, nucleic acids, unnatured drugs) in biological samples. Nowadays, the new era of personalized medicine and healthcare intelligence is further promoting the development of analytical technologies, especially calling for the replacement of traditional manual analysis with automated and high-throughput machine operations. The emerging field of microfluidics offers a potential solution to miniaturizing and automating traditional analytical methods, where frequently repeated liquid handling operations (e.g., metering, mixing, extraction) can be programmed and processed on a microfluidic device. However, laboratory automation of these delicate devices is hampered by a lack of world-to-chip interfaces and the complexity of external infrastructure settings. In this dissertation, we introduced a universal robotic-fluidic interface (RoMI) and modular microfluidic design for fully automated microfluidics in biomedical applications. Our research projects include: 1) establishing and validating the RoMI platform through a droplet dispensing module; 2) developing a multiplexed strategy for protein network studies *in vitro* using the RoMI platform and a customized droplet dispensing module; 3) developing a human-free sample-to-answer ELISA system using the RoMI platform and a hybrid microfluidic module. With its modular connectivity, high adaptability, and multitasking capacity, RoMI can be used to drive a variety of microfluidic modules in a simply programmable manner with minimal external infrastructure requirements. Overall, the newly developed RoMI has displayed significant promise in promoting the usability and flexibility of microfluidic technology in biomedical analyses, allowing for new opportunities and insights in the next generations of laboratory automation.

Paper permission in this dissertation:

Reproduced with permission from “Microfluidic cap-to-dispense (μCD): a universal microfluidic–robotic interface for automated pipette-free high-precision liquid handling” by J. Wang, K. Deng, C. Zhou, Z. Fang, C. Meyer, K. U. Deshpande, Z. Li, X. Mi, Q. Luo, B. D. Hammock, C. Tan, Y. Chen and T. Pan, Lab Chip, 2019, 19, 3405, Copyright [2019] by Royal Society of Chemistry.

Reproduced with permission from “Building protein networks in synthetic systems from the bottom-up” by J. Shim, C. Zhou, Ting Gong, D. A. Iserlis, H. A. Linjawi, M. Wong, T. Pan, C. Tan, Biotechnology Advances, Volume 49, July–August 2021, 107753, Copyright [2021] by Elsevier.

Reproduced with permission from “Sample-to-Answer Robotic ELISA” by C. Zhou, Z. Fang, C. Zhao, X. Mai, S. Emami, A. Y. Taha, G. Sun, and T. Pan, Analytical Chemistry, 2021, 93, 11424−11432, Copyright [2021] American Chemical Society.

Reproduced from “The engineering of a microfluidic printing robot for protein network reconstitution” by C. Zhou, J. Shim, Z. Fang, C. Meyer, T. Gong, M. Wong, C. Tan and T. Pan (in submission). The copyright of the final publication resides with the authors or the publisher depending on the publisher's business model.

Table of Contents

List of Figures

List of Tables

Chapter 1 Introduction

1.1 Background

1.1.1 RoMI for automated low-volume liquid handling

Liquid handling is an essential step involved in almost all laboratory procedures for contemporary life sciences and medical studies. These include polymerase chain reaction (PCR), immunoassays, and drug screening; where biological or clinical samples have to be frequently transferred between storage containers or dispensed onto analytical substrates. (Kong et al., 2012; Oosterbroek and van den Berg, 2003) With the new advent of precision and personalized medicine, the demand for handling minute volumes of samples has increased drastically. For instance, a large array of combinatorial assays often have to be prepared and screened with sensitive and precious samples in synthetic biological studies (Harris and Jewett, 2012; Villarreal et al., 2018; Villarreal and Tan, 2017) and combinatorial drug therapies (Al-Lazikani et al., 2012; Beltran et al., 2011). In these studies traditional manual procedures of liquid handling using micropipettes is cumbersome and impractical. (Art et al., 2016) To minimize analytical errors and improve the operational efficiencies, further technical advancement is essential for liquid handling methods with higher precision, lower volume processing capacity, and negligible human-induced errors and interruptions. (Derby, 2008; Ding et al., 2013; Dunn and Feygin, 2000)

To overcome the human errors involved in the traditional manual operations, an array of automated liquid handling workstations have been developed in the last couple of decades to resemble the pipetting function using a robotic interface. (Feature, 2008; Lorenz, 2004; Mathes and Parker, 2017) In general, piston-driven single channel or multichannel micropipettes are mounted onto a high-precision 3-axis traveling stage (e.g., Fluent™ from Tecan and OT-2™ from Opentrons), which directs the spatial movements and positioning, and can be programmed to automate a number of repetitive protocols and workflows, resembling the manual pipetting procedures. (Mattheakis, 2014; Scott-brown and Papachristodoulou, 2017) Benefiting from the rapid development of industrial robots, the concept of co-robots has been recently introduced with the purpose of laboratory automation. The idea is to offer more flexible and adaptive operations compared to their existing counterparts. These labor-saving robotic devices aim to improve the productivity and throughput of routine and repetitive work, while offering the capacity to work with laboratory personnel and research staff side-by-side. These processes will be accompanied by injury preventing sensors and embedded protocols. (Liu and Tomizuka, 2016) A new variety of pipetting-manipulating co-robots have been devised and added to the family of liquid-handling equipment, such as Mantis from Formulatrix and ReadyGo from BioWavelet. (Mitchell et al., 2015; O'Connell et al., 2014)

Although encouraging progress has been demonstrated by adopting robotic automation to liquid handling in both industry and academia, one major limitation of this approach remains inadequately addressed, namely the accuracy of low-volume (sub-microliter) processing. Moreover, the intrinsic differences between human-pipette and machine-pipette interfaces have been largely overlooked, aside from marginal modifications, thereby creating further barriers to automate additional human-centric operations. (Chen and Pan, 2011; Fan et al., 2018; Fredrickson and Fan, 2004) Additionally, to address such a growing demand in ultralow-volume liquid handling, nanoliter or picoliter dispensing technologies have been quickly adopted from the inkjet printing industry. (Cheng et al., 2005; Cooley et al., 2002; Dunn and Feygin, 2000; Sirringhaus et al., 2000) While the pipetting method always results in a residual volume on the pipette tips and leads to inaccuracy in a low-volume setting, inkjet printing is able to eject liquid from a small orifice by utilizing a precisely-controlled driving force to overcome the surface tension and ensure accuracy of liquid volumes. (Jacot-Descombes et al., 2012; Oosterbroek and van den Berg, 2003; Zakir Hossain et al., 2009) Both the do-it-yourself method by modifying from an off-the-shelf inkjet printer (e.g., PIXMA iP1300 from Canon, and K100 from EPSON)(Hong et al., 2015; Oh et al., 2013; Yoshioka and Jabbour, 2006) and the commercial solutions of a high-precision dispenser (e.g. Dimatix from Fujifilm, and D300 from Tecan)(Alkasir et al., 2012; Brennan-Krohn et al., 2017; Di Risio and Yan, 2007; Reis et al., 2005) have become widely employed in sub-microliter dispensing. However, the existing high-precision dispensing nozzles either require an expensive integrated piezoelectric actuator to achieve the dispensing precision, which typically involves complicated manufacturing process, (Li et al., 2015) or relies on a thermal expansion approach, which is incompatible with many biological systems. (Derby, 2008) Additionally, these high-cost dispensers prohibit their application for disposable uses, and cumbersome washing and cleaning is required to minimize cross-contamination between uses. (Antohe and Cooley, 2007; Ding et al., 2013) Moreover, the connection to the dispenser head is rather conventional, using extensive classical tubing and fitting connections, resulting in large loading and dead volumes, considerable waste of precious reagents, and difficulties when changing reagents and samples. (Fan et al., 2017; Setti et al., 2005; Zakir Hossain et al., 2009) Meanwhile, ultralow-volume liquid handling could also be realized by pneumatic drive. Miniature droplets could be generated by pulsed pneumatic pressure. The frequency of pulse waves in the droplet generator can be tunable by the pulse duration, nozzle size and driving pressure. (Cheng and Chandra, 2003) The pneumatic valve implemented next to the microfluidic T-junction can produce arrays of uniform emulsion droplets in various sizes in a high throughput manner. (Choi et al., 2010) In our previous studies, we have shown that pneumatic droplet generation method has great potential in biological and chemical studies, since the droplets size could be highly controllable using the tunable geometrical and pneumatic parameters. (Li et al., 2018a, 2018b)

Recently, microfluidic-derived dispensing technologies, also known as microfluidic adaptive printing (MAP), have been established to generate picoliter and nanoliter droplets on-demand. By separating the actuating mechanism from the liquid-containing cartridge, the microfluidic printing has the advantages of simple fabrication, inexpensive construction, non-contact dispensing, and flexible multiplexing, allowing a low-cost alternative to existing nanoliter dispensing solutions. (Leung et al., 2012) In our original work on MAP, we have designed and fabricated an interchangeable microfluidic cartridge with multiplexed sample channels, driven by a dot-matrix printer head, featuring a low loading volume of 0.6 µL and a dead volume of 0.05 µL. (Ding et al., 2015, 2013) By utilizing both piezoelectric and pneumatic drives, MAP printing achieves linear scalability, high frequency, and tunable droplet generation. It has been successfully employed in multi-parametric gene regulatory studies and combinatorial peptide microarray synthesis. (Fan et al., 2017; Li et al., 2019, 2018a, 2018b; Villarreal et al., 2018) More recently, several high-precision sub-microliter pipetting systems using the MAP mechanism have been introduced with disposable microfluidic pipetting tips. (Choi et al., 2015; Fan et al., 2018; Mao et al., 2018; Zhang et al., 2016) Although existing studies have illustrated the potential of integrating microfluidic printing with a commercial micropipette to achieve high precision and on-demand nanoliter volume dispensing, the functions of such devices are limited to dispensing only, while the interface between the machine and the pipette tips remains unchanged. Therefore, the lack of world-to-chip (macro-to-micro) connectivity still prevents complete automation.

In this dissertation, we introduce the first pipette-free robotic-dispensing interface using a microfluidic-enabled container cap, referred to as a Microfluidic Cap-to-Dispense (µCD) which achieves a seamless integration of liquid handling and robotic operations. The new pipette-free microfluidic-robotic interface offers a simple and modular way to connect the robotic drive with a standard liquid container, exploiting the high accuracy and high flexibility of the robotic recognition and motion system to achieve high-precision on-demand volume dispensing by microfluidic adaptive printing. In brief, this novel microfluidic liquid-handling system includes multiple functions for laboratory automation in a complete automated solution, namely target/sample recognition, container catch-and-release, positioning, high-precision dispensing, and multiplexing. As the core of the µCD concept, the multilayer-assembled microfluidic cap consists of a microfluidic printing nozzle, a tube connector, and two pneumatic control channels reversibly linked to the robotic effector upon contact. In addition, the robotic effector has been custom-modified to grab the liquid container, but also contains the pneumatic drive to power the microfluidic cap through the contact interface. As a demonstration, we have employed the µCD system to fully automate the characterization of a synthetic genetic circuit, in which multi-dimensional analyses of two regulatory factors have been investigated in high throughput with low consumption of reagents, yielding an optimized condition for the selected genetic expression process. This experiment can be easily modified and adapted to similar combinatorial biological processes. Compared with serial dilutions typically operated by manual pipettes in most biological labs, our system improves the efficiency and accuracy of multifactorial studies with a wide range of concentrations. With its modular connectivity, nanoliter processability, high adaptability, and multitask capacity, µCD has shown a great potential as a generic robotic platform for future pipette-free laboratory automation.

1.1.2 RoMI enabled protein network reconstitution

Recent work has reconstituted protein networks *in vitro*, where at least two purified catalytic compounds (enzymes and proteins) are put together to investigate how they affect each other and give rise to a cellular function of interest.(dos Santos et al., 2020; Garni et al., 2018) The emerging studies of protein networks are becoming important for various applications, for instance, switching on/off biological transduction pathways(Hui and Vale, 2014; Su et al., 2016), developing energy self-supplying systems(Berhanu et al., 2019; Miller et al., 2020), and screening peptide-based drugs(Cui et al., 2016). Conventionally, the biochemical study of proteins is carried out using well plates and manual pipetting. Due to the increasing demands for quantitation, efficiency, and convenience of detection, a number of liquid handling robotic workstations (e.g., Biomek® 3000 from Beckman Coulter and Microlab® STAR from Hamilton), together with fluorescent biosensing technologies(Morris, 2013), have been developed to study protein reactions in well plates (96 to 1536).(Kong et al., 2012; Smith, 2007) The power of automated robotic workstations is evident in improving the capacity of sample handling and the reproducibility of analytical results while reducing human errors and saving hands-on time.(Kong et al., 2012; Wang et al., 2019) However, the liquid handling volume of these workstations usually ranges from a few to hundreds of microliters. Thus, the reagent cost is considerable for quantitative protein network studies that consist of thousands of protein network reactions. In addition, the well plate-based methods have intrinsic fundamental limitations for the assembly of the protein network. As revealed recently, protein kinase reactions in solution (well plate-based) is different from that in cell-mimicking vesicles, mainly due to the membrane confinement or attachment.(Gureasko et al., 2008; Hui and Vale, 2014; Wang et al., 1992)

To minimize the reagent consumption and mimic the cell membrane confinement *in vitro*, droplet microfluidics is emerging as the next-generation platform for the construction of biomimetic cells. It enables the encapsulation of multiple biomolecular reagents in water-in-oil droplets in spherical micrometer-sized compartments and therefore mimics the environment of natural cells.(Shim et al., 2021) For instance, a cross junction-based microfluidic design has been successfully used for the encapsulation of hybrid synthetic chloroplasts(Miller et al., 2020) and DNA fragments with the IVT2H reagents(Cui et al., 2016) in droplets in high throughput. Furthermore, a six-way junction-based droplet-generating device has been demonstrated for the study of a three-enzyme (β-gal, GOx, and HRP) combinatorial biochemical pathways.(dos Santos et al., 2020) Such studies have validated the benefits of reconstituting biological pathways using droplet microfluidics, demonstrating features such as high-frequency, high encapsulation efficiency, and precise size control. However, it remains challenging for conventional droplet microfluidic devices to flexibly vary the droplet contents on demand.(Abate et al., 2010; Rane et al., 2015) To this end, picoliter/nanoliter injection technologies have been lately employed for combinatorial screening applications. For instance, Weiss and his co-workers have designed injection channels downstream of a vesicle-encapsulation channel. They used a high voltage to induce the fusion of the reagent from the injection channel into the vesicle, and they have successfully tuned the injected volume by varying the pressure in the injection channel.19-20 In another example, Rane's group has employed a valve-based droplet generation method for reagent injection and droplet displacement operations in a microfluidic device, and they have adjusted the reagent injection volume and concentration in a droplet by tuning the duration of valve opening.(Rane et al., 2015) However, such on-chip injection devices need delicate control equipment for each individual channel, thus it is difficult to scale up for multi-parametric screening. Besides, extra efforts are required to distinguish different droplets using techniques such as injecting labeling reagents or designing a lengthy incubation channel. Therefore, the current droplet microfluidics-based platforms are still challenging for the quantitative studies of protein networks.

Recently, our group has developed a novel microfluidic adaptive printing (MAP) platform to generate droplets in air, in contrast to the conventional droplet-in-oil channel-based microfluidic devices.(Ding et al., 2013b) We have combined it with cell-free systems to enable multi-parametric studies of genetic promoters, and achieved combinatorial studies of the reagents conveniently through the adaptive droplet printing. In this dissertation, we built on our prior work and engineered a microfluidic printing robot for a novel two-step process assembly of protein networks in different concentration profiles. The robot enables us to compare target protein(s) in both unbound-state and bound-state (to a lipid membrane) simultaneously. In the first step, we utilize our previously developed microfluidic pipette-free robot that incorporated with a robotic-microfluidic interface (RoMI) to handle multiple microfluidic cartridges to generate multiplexed droplet arrays on a hydrophobic substrate, seamlessly integrating the modular microfluidic cartridges with robotic operations for the automated low volume pipetting.(Wang et al., 2019) Notably, these microfluidic cartridges are inexpensive and disposable, with an accuracy of 93.8 % in generating 59.2 nL single droplets. In the second step, phospholipid-dissolved oil is poured over the droplet arrays to form a lipid membrane surrounding the preformed droplets. In addition, anchor lipids DGS-NTA(Ni) are selectively added into the oil, allowing for the specific bindings between the lipid membrane and his-tagged proteins inside the preformed droplet. As a demonstration, we assemble a sub-network of mitogen-activated protein kinase (MAPK) containing MEK or/and ERK kinase. Around 100 droplets with different protein concentrations have been prepared within 10 min, in which the droplet size (1 μL) is 1-2 orders of magnitude lower than that of the conventional well plate-based protein network reactions. We also study the activities of both unbound and bound kinases simultaneously. Benefiting from its high multiplexing capacity, disposable cartridges design, cell-mimicking reaction environment, and selective lipid-protein binding, our robotic system can be applied for broad protein network research.

1.1.3 RoMI enabled automated ELISA

Immunoassays, as one of the most commonly used biochemical tests, have been conducted ubiquitously in hospitals, research laboratories, etc. (Vinet and Zhedanov, 2011) Since its origination in the 1950s, immunoassays have become the most commercially successful diagnostic technology, covering applications from home pregnancy testing to AIDS testing and to the most recent COVID-19 diagnosis, etc. (Carter et al., 2020; Vinet and Zhedanov, 2011) It typically relies on a specific and strong interaction between an antibody and an antigen to detect a potential target analyte, which ranges from natural and man-made chemicals, biomolecules, cells to viral particles, etc. (Vinet and Zhedanov, 2011) Specifically, a classic immunoassay consists of three components, namely an antibody, an analyte (antigen), and a detectable label for the indication and signaling of the antibody-antigen binding events. Thus, the immunoassays can be classified into multiple types according to the various forms of labels, including enzymes, radioactive isotopes, fluorophore, chemiluminescent probes, microbeads, and nanoparticles, etc. Among them, the most popular labels used are enzymatic types, owe to the simple molecular design in the overall assay; and the corresponding enzyme-linked immunosorbent assays (ELISA), therefore, have become the most common immunoassay. Notably, almost all existing diagnostic laboratories may have already encountered at least one form of ELISA tests. (Lequin, 2005; Vinet and Zhedanov, 2011) In its simplest form, the conventional ELISA contains solid-phase reactions between an antibody (Ab) immobilized on a solid-phase platform (e.g., 96 well microtiter plates) and an antigen (Ag) in a liquid sample. (Vinet and Zhedanov, 2011) Despite its advantages including simplicity in design and high sensitivity in detection, the conventional manually operated ELISA has experienced some major drawbacks. For instance, the assay procedure is usually laborious since it involves multiple liquid pipetting, washing, and incubation steps, in addition to the lengthy reaction time involved. (Hosseini et al., 2018) Moreover, it relies considerably on the skills of technicians, which becomes critical to obtain consistent results. (Hosseini et al., 2018) Finally, the heavy human involvement requires numerous administrative and regulatory efforts in the procedure to minimize the harms of a target analyte that could be toxic, infectious, and sometimes even fatal to the operators. Such limitations of the conventional ELISA procedure call for innovations to automate the multiple liquid handling and readout steps and eventually eliminate the participation of humans, ideally leading to a fully automated human-free ELISA procedure. (Hosseini et al., 2018)

The commercial automation efforts for ELISA operations have been primarily focused on the standard well plate platforms. Some of the representative automated ELISA systems are shown in Table 1-1. A range of specialized instruments have been designed to fit the microwell plates, such as robotic pipetting devices, washers, shakers, incubators, and microtiter plate readers. More recently, fully automated ELISA systems have been implemented to integrate the aforementioned components into one piece of equipment. Representative commercial products include Freedom EVO® ELISA Biopharma from Tecan, Crocodile ELISA miniWorkstation from BERTHOLD TECHNOLOGIES, ELISA STARlet from HAMILTON Robotics, and Agility® ELISA from Abbott, etc. Although such systems have enabled the fully automated functions of the ELISA procedure and some of them are capable of processing up to hundreds of samples at a time, they typically possess a large footprint and are expensive to acquire, and thus, are not intended to be used in the research laboratories or resource-limited clinics. Furthermore, these conventional well plate-based platforms have relatively low efficacies of molecular adsorptions and the correspondingly low sensitivity of readouts due to the limited surface-to-volume ratio of the wells. (Hosseini et al., 2018)

As an emerging transformative technology, microfluidics has begun to reshape the conventional bioanalytical fields, including ELISA systems, over the past decades, with the potential to offer 1) affordability, 2) sensitivity, 3) specificity, 4) user-friendliness, 5) rapid and robust, 6) equipment-free, and 7) deliverable to those in need for such technologies, as outlined by the World Health Organization (WHO). (Peeling et al., 2006) Table 1-1 features a group of representative microfluidic-enabled ELISA automation systems. Based on the primary constructive materials, the automated microfluidic ELISA systems could be categorized into polymeric, paper-based, or hybrid devices. Among them, the polymeric ELISA chips employ various mechanisms for liquid handling, including capillary force (Khodayari Bavil and Kim, 2018b), centrifugal force (Lee et al., 2009b), off-the-chip (Yang et al., 2011) or integrated pumps and valves (Kim et al., 2011; Zheng et al., 2012), sequential delivery of liquid segments (Chin et al., 2011; Song et al., 2016). Lee's group have designed a fully automated disc-shaped microfluidic ELISA system for the detection of infectious diseases from the whole blood, with microbead-based suspensions, in which plasma separation, incubation, washing, and enzyme reaction have been incorporated. (Lee et al., 2009b) Moreover, Qin's group have employed the SlipChip technology to generate liquid segments followed by flowing into the ELISA wells under a vacuum pressure generated by a pipette. (Song et al., 2016) As manifested in Table 1-1, such microfluidic ELISA platforms miniaturize the whole system, remove the dedicated control equipment, reduce the duration of assays, and enhance the detection sensitivity, as compared to that of the conventional plate-based ELISA. (Sanjay et al., 2020) However, the current polymeric microfluidic chips require extended

Table 1-1 Comparisons of current automation schemes of ELISA

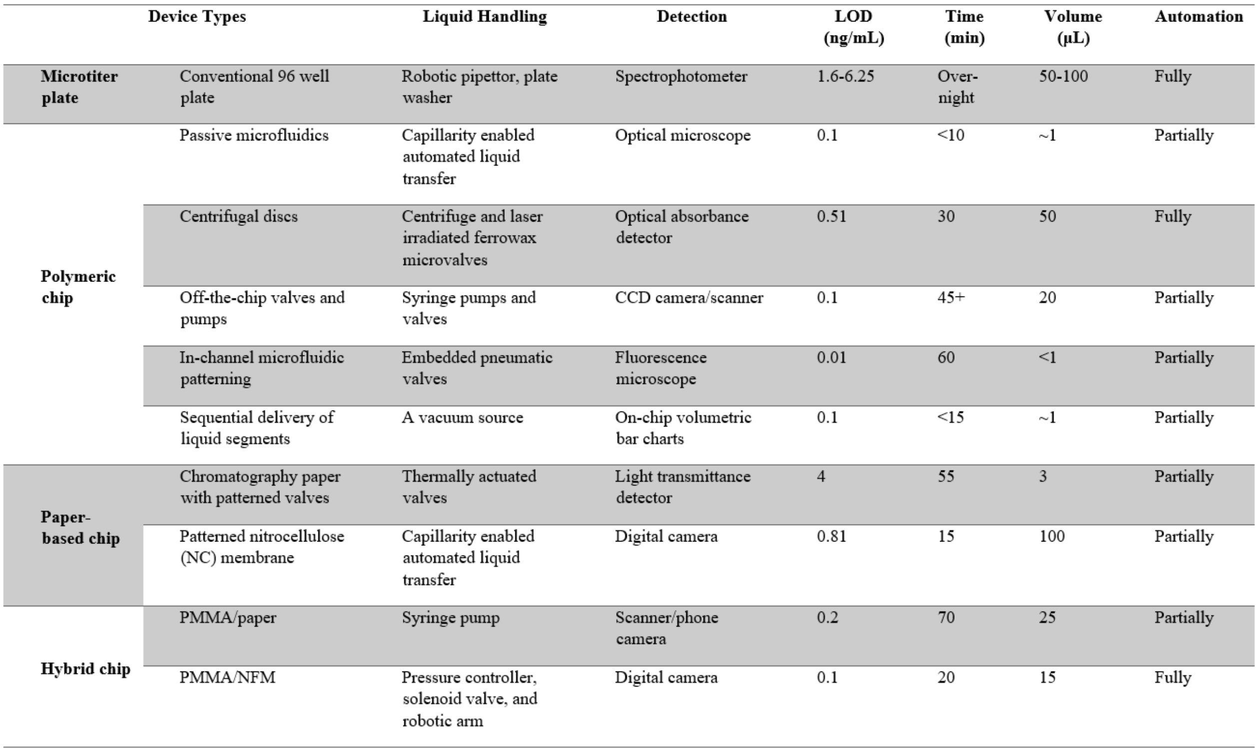

Device Types		Liquid Handling	Detection	LOD (ng/mL)	Time (min)	Volume (µL)	Automation
Microtiter plate	Conventional 96 well plate	Robotic pipettor, plate washer	Spectrophotometer	1.6-6.25	Over-night	50-100	Fully
Polymeric chip	Passive microfluidics	Capillarity enabled automated liquid transfer	Optical microscope	0.1	<10	~1	Partially
	Centrifugal discs	Centrifuge and laser irradiated ferrowax microvalves	Optical absorbance detector	0.51	30	50	Fully
	Off-the-chip valves and pumps	Syringe pumps and valves	CCD camera/scanner	0.1	45+	20	Partially
	In-channel microfluidic patterning	Embedded pneumatic valves	Fluorescence microscope	0.01	60	<1	Partially
	Sequential delivery of liquid segments	A vacuum source	On-chip volumetric bar charts	0.1	<15	~1	Partially
Paper-based chip	Chromatography paper with patterned valves	Thermally actuated valves	Light transmittance detector	4	55	3	Partially
	Patterned nitrocellulose (NC) membrane	Capillarity enabled automated liquid transfer	Digital camera	0.81	15	100	Partially
Hybrid chip	PMMA/paper	Syringe pump	Scanner/phone camera	0.2	70	25	Partially
	PMMA/NFM	Pressure controller, solenoid valve, and robotic arm	Digital camera	0.1	20	15	Fully

(References from the top to the bottom are: Sanjay et al., 2020, Khodayari Bavil and Kim, 2018, Lee et al., 2009, Yang et al., 2011, Zheng et al., 2012, Song et al., 2016, Fu et al., 2019, Apilux et al., 2013, Sanjay et al., 2020 and this work)

development cycles and complex fabrication procedures with a high production cost, in addition to the limited flexibility configured for multi-purposes. Moreover, the surface area of the microchannel is limited to effective protein bindings. Furthermore, the world-to-chip interface is another major challenge to the laboratory automation of such microfluidic devices. (Yuen and Goral, 2010)

Alternatively, the paper-based microfluidic devices have appreciably more surface area available for Ab-Ag binding, benefiting from their intrinsic 3D nanoscopic topology. They are cost-effective, and therefore, can be readily deployed in resource-limited settings. (Li et al., 2020) One pioneer work in the automation of paper-based ELISA have been proposed by Chailapakul, Takamura and their colleagues, which has patterned flow barriers on a nitrocellulose (NC) paper for the control of fluid flow and used capillarity for the purely passive automatic loading of the liquid onto the paper, thus eliminating any external dedicated instrument for flow control. (Apilux et al., 2013) Despite of the increased binding sites and the device simplicity, the paper-based ELISA methods have shown limited sensitivity compared to the polymeric devices, largely due to the restricted hydrodynamic forces under the purely passive capillary-driven flow. (Khodayari Bavil and Kim, 2018b) Recently, a nanofibrous membrane (NFM)-based ELISA system has been presented, utilizing an extremely high surface-to-volume ratio of NFM for the efficient Ab immobilization, which has been proven with a significantly higher sensitivity than that of the conventional NC papers. (Zhao et al., 2020) With such efficient immobilization, the NFM-based ELISA device has enabled naked-eye colorimetric detection at a limit of detection as low as 0.3 ng/mL, within a rapid incubation window of 5 min. (Zhao et al., 2020) However, the emerging NFM-based ELISA system has yet to be automated, mainly due to the lack of solutions to handle and manipulate the NFM substrates automatically and conveniently.

By combining the features of both the polymeric and the paper-based devices, the hybrid ELISA chip offers additional advantages over its predecessors. In one recent work by Li's group, a reusable PMMA/paper hybrid device has been designed to be plug-and-play, resulting in a demonstration for high-sensitivity and low-limit detection of immunoglobulin G (IgG) down to 0.2 ng/mL. (Sanjay et al., 2020) In particular, a pre-patterned paper is inserted into a simplified PMMA microfluidic device with preset slots, and the sample is then infused into the device to flow back-and-forth through the paper, enabling enhanced analyte enrichment and efficient washing. (Sanjay et al., 2020) Although various studies have significantly improved sensitivities and expanded dynamic ranges of hybrid microfluidic devices to the conventional ELISA operations, the current approaches are still far from being fully automated. For instance, an external flow drive (e.g., a syringe pump) is needed to attach to the system, while the microfluidic chip has to be manually placed for scanned readout.

Recently, our group has introduced the first modular robotic-microfluidic interface (RoMI) for the world-to-chip bridging. The fully automated manipulation of the modular microfluidic devices using a standard robotic arm has been implemented with operations such as recognition, capturing, positioning, and liquid handling. (Wang et al., 2019) In this dissertation, we have extended the RoMI platform for the automation of ELISA, referred to as Robotic ELISA, by incorporating a modular microfluidic chip that embeds the aforementioned ultrasensitive NFM-based biosensor into a layer-by-layer polymeric construct. The fully automated robotic system is intended to carry out multiple bioanalytical procedures to replace all the manual steps involved in classic ELISA operations, including the pneumatically driven high-precision pipetting, mixing, efficient washing, as well as integrated machine vision for colorimetric readout, leading to a facile human-free sample-to-answer workflow of ELISA. Moreover, the microfluidic chip is designed to accommodate a standard modular fabrication procedure and assembled layer-by-layer into an integrated device, which can be captured and released by the robotic effector reversibly. Benefiting from the modular microfluidic design, the automated back-and-forth flows of the liquid samples and subsequent reagents through the NFM sensors have been achieved, and as a result, the Ab-Ag binding efficacy and the overall sensitivity has been significantly improved, relative to that of the manual operations of the same procedure. (Zhao et al., 2020) As a demonstration, we have successfully applied the Robotic ELISA platform to the automated detection of chloramphenicol (CAP). All of the ELISA operations from sample preparation to signal readout have been automatically completed within 20 min without human intervention, of which the reaction volume (15 μL) is an order of magnitude lower than that of the conventional ELISA methods using 96-well plates, and the limit of detection (LOD) achieved is 0.1 ng/mL. Benefiting from its modular design and automated operations, the Robotic ELISA platform could be potentially deployed for a broad range of detections in resource-limited settings or high-risk environments, where human involvement needs to be minimized, while the testing timeliness, consistency and sensitivity are all desired.

1.2 Objective, Significance, and Innovation

The overall goal of this dissertation is to build a universal Robot-Microfluidic Interface (RoMI) that can handle various microfluidic modules, thus enabling programmable and fully automated biochemical analyses. The first objective is to design and fabricate a pair of RoMI connectors mounted on the end-effectors of the robotic arms. By opening and closing the robotic arms, a seamless and reversible connection between the robot and the microfluidic module could be used for multi-module tasks with minimized off-chip components. In addition, we have designed and fabricated a droplet printing module by employing our previously developed microfluidic adaptive printing technology. With this, RoMI could realize fully automated, high-precision, low-volume liquid handling by operating printing modules that preloaded with different reagents. The second objective is to apply the developed RoMI and the printing module in multiplexed protein network studies. To further simulate the cell environment, phospholipids-dissolving oil is added to form a lipid membrane layer on the surface of the droplets. This case study shows the great potential of RoMI in promoting the understanding of the reaction mechanism of protein networks in natural cells. The third objective is to employ RoMI to automate a novel nanofibrous membrane-based microfluidic ELISA module. The target analyte could be detected in a fully automated sample-to-answer manner within 20 minutes.

In summary, the objective is to develop an innovative laboratory robot, RoMI, that can 1) employ robotics to automate microfluidics; 2) adapt to a variety of microfluidic module designs; 3) minimize the use of off-chip components; 4) be open-source and easy-to-use for the entire biochemical community. As microfluidic technology plays an increasingly important role in molecular detection, RoMI has the potential to become a leading laboratory robot that can introduce the latest microfluidic technologies into biomedical analyses in a simply automated and programmable manner.

References

Abate, A.R., Hung, T., Mary, P., Agresti, J.J., Weitz, D.A., 2010. High-throughput injection with microfluidics using picoinjectors. Proc. Natl. Acad. Sci. https://doi.org/10.1073/pnas.1006888107

Al-Lazikani, B., Banerji, U., Workman, P., 2012. Combinatorial drug therapy for cancer in the post-genomic era. Nat. Biotechnol. https://doi.org/10.1038/nbt.2284

Alkasir, R.S.J., Ornatska, M., Andreescu, S., 2012. Colorimetric paper bioassay for the detection of phenolic compounds. Anal. Chem. 84, 9729–9737. https://doi.org/10.1021/ac301110d

Antohe, B. V., Cooley, P.W., 2007. In situ synthesis of peptide microarrays using ink-jet microdispensing. Methods Mol. Biol. 381, 299–312. https://doi.org/10.1385/1-59745-303-X:299

Apilux, A., Ukita, Y., Chikae, M., Chailapakul, O., Takamura, Y., 2013. Development of automated paper-based devices for sequential multistep sandwich enzyme-linked immunosorbent assays using inkjet printing. Lab Chip 13, 126–135. https://doi.org/10.1039/c2lc40690j

Art, M., Dufey, V., Gast, U., Gligor, I., Koch, L., Kubasch, R., 2016. The Tip of the Iceberg : How Pipette Tips Influence Results. Nat. Methods 1–22.

Beltran, H., Beer, T.M., Carducci, M.A., De Bono, J., Gleave, M., Hussain, M., Kelly, W.K., Saad, F., Sternberg, C., Tagawa, S.T., Tannock, I.F., 2011. New therapies for castration-resistant prostate cancer: Efficacy and safety. Eur. Urol. https://doi.org/10.1016/j.eururo.2011.04.038

Berhanu, S., Ueda, T., Kuruma, Y., 2019. Artificial photosynthetic cell producing energy for protein synthesis. Nat. Commun. https://doi.org/10.1038/s41467-019-09147-4

Brennan-Krohn, T., Truelson, K.A., Smith, K.P., Kirby, J.E., 2017. Screening for synergistic activity of antimicrobial combinations against carbapenem-resistant Enterobacteriaceae using inkjet printer-based technology. J. Antimicrob. Chemother. 72, 2775–2781. https://doi.org/10.1093/jac/dkx241

Carter, L.J., Garner, L. V., Smoot, J.W., Li, Y., Zhou, Q., Saveson, C.J., Sasso, J.M., Gregg, A.C., Soares, D.J., Beskid, T.R., Jervey, S.R., Liu, C., 2020. Assay Techniques and Test Development for COVID-19 Diagnosis. ACS Cent. Sci. 6, 591–605. https://doi.org/10.1021/acscentsci.0c00501

Chen, A., Pan, T., 2011. Fit-to-Flow (F2F) interconnects: Universal reversible adhesive-free microfluidic adaptors for lab-on-a-chip systems. Lab Chip 11, 727–732. https://doi.org/10.1039/c0lc00384k

Cheng, S., Chandra, S., 2003. A pneumatic droplet-on-demand generator. Exp. Fluids 34, 755–762. https://doi.org/10.1007/s00348-003-0629-6

Cheng, S.X., Li, T., Chandra, S., 2005. Producing molten metal droplets with a pneumatic droplet-on-demand generator. J. Mater. Process. Technol. 159, 295–302. https://doi.org/10.1016/j.jmatprotec.2004.05.016

Chin, C.D., Laksanasopin, T., Cheung, Y.K., Steinmiller, D., Linder, V., Parsa, H., Wang, J., Moore, H., Rouse, R., Umviligihozo, G., Karita, E., Mwambarangwe, L., Braunstein, S.L., Van De Wijgert, J., Sahabo, R., Justman, J.E., El-Sadr, W., Sia, S.K., 2011. Microfluidics-based diagnostics of infectious diseases in the developing world. Nat. Med. https://doi.org/10.1038/nm.2408

Choi, I.H., Kim, H., Lee, S., Baek, S., Kim, J., 2015. Plug-in nanoliter pneumatic liquid dispenser with nozzle design flexibility. Biomicrofluidics 9. https://doi.org/10.1063/1.4935937

Choi, J.H., Lee, S.K., Lim, J.M., Yang, S.M., Yi, G.R., 2010. Designed pneumatic valve actuators for controlled droplet breakup and generation. Lab Chip 10, 456–461. https://doi.org/10.1039/b915596a

Cooley, P., Wallace, D., Antohe, B., 2002. Applications of ink-jet printing technology to BioMEMS and microfluidic systems. JALA - J. Assoc. Lab. Autom. https://doi.org/10.1016/S1535-5535(04)00214-X

Cui, N., Zhang, H., Schneider, N., Tao, Y., Asahara, H., Sun, Z., Cai, Y., Koehler, S.A., De Greef, T.F.A., Abbaspourrad, A., Weitz, D.A., Chong, S., 2016. A mix-and-read drop-based in vitro two-hybrid method for screening high-affinity peptide binders. Sci. Rep. https://doi.org/10.1038/srep22575

Derby, B., 2008. Bioprinting: Inkjet printing proteins and hybrid cell-containing materials and structures. J. Mater. Chem. 18, 5717–5721. https://doi.org/10.1039/b807560c

Di Risio, S., Yan, N., 2007. Piezoelectric ink-jet printing of horseradish peroxidase: Effect of ink viscosity modifiers on activity. Macromol. Rapid Commun. 28, 1934–1940. https://doi.org/10.1002/marc.200700226

Ding, Y., Huang, E., Lam, K.S., Pan, T., 2013a. Microfluidic impact printer with interchangeable cartridges for versatile non-contact multiplexed micropatterning. Lab Chip 13, 1902–1910. https://doi.org/10.1039/c3lc41372a

Ding, Y., Huang, E., Lam, K.S., Pan, T., 2013b. Microfluidic impact printer with interchangeable cartridges for versatile non-contact multiplexed micropatterning. Lab Chip. https://doi.org/10.1039/c3lc41372a

Ding, Y., Li, J., Xiao, W., Xiao, K., Lee, J., Bhardwaj, U., Zhu, Z., Digiglio, P., Yang, G., Lam, K.S., Pan, T., 2015. Microfluidic-Enabled Print-to-Screen Platform for High-Throughput Screening of Combinatorial Chemotherapy. Anal. Chem. 87, 10166–10171. https://doi.org/10.1021/acs.analchem.5b00826

dos Santos, E.C., Belluati, A., Necula, D., Scherrer, D., Meyer, C.E., Wehr, R.P., Lörtscher, E., Palivan, C.G., Meier, W., 2020. Combinatorial Strategy for Studying Biochemical Pathways in Double Emulsion Templated Cell-Sized Compartments. Adv. Mater. 32. https://doi.org/10.1002/adma.202004804

Dunn, D.A., Feygin, I., 2000. Challenges and solutions to ultra-high-throughput screening assay miniaturization: Submicroliter fluid handling. Drug Discov. Today 5, S84–S91. https://doi.org/10.1016/S1359-6446(00)80089-6

Fan, J., Men, Y., Hao Tseng, K., Ding, Yi, Ding, Yunfeng, Villarreal, F., Tan, C., Li, B., Pan, T., 2018. Dotette: Programmable, high-precision, plug-and-play droplet pipetting. Biomicrofluidics 12. https://doi.org/10.1063/1.5030629

Fan, J., Villarreal, F., Weyers, B., Ding, Y., Tseng, K.H., Li, J., Li, B., Tan, C., Pan, T., 2017. Multi-dimensional studies of synthetic genetic promoters enabled by microfluidic impact printing. Lab Chip 17, 2198–2207. https://doi.org/10.1039/c7lc00382j

Feature, T., 2008. Lab automation: tales along the road to automation. Nat. Methods 5, 109–112.

Fredrickson, C.K., Fan, Z.H., 2004. Macro-to-micro interfaces for microfluidic devices. Lab Chip 4, 526–533. https://doi.org/10.1039/b410720a

Fu, H., Song, P., Wu, Q., Zhao, C., Pan, P., Li, X., Li-Jessen, N.Y.K., Liu, X., 2019. A paper-based microfluidic platform with shape-memory-polymer-actuated fluid valves for automated multi-step immunoassays. Microsystems Nanoeng. https://doi.org/10.1038/s41378-019-0091-0

Garni, M., Einfalt, T., Goers, R., Palivan, C.G., Meier, W., 2018. Live Follow-Up of Enzymatic Reactions Inside the Cavities of Synthetic Giant Unilamellar Vesicles Equipped with Membrane Proteins Mimicking Cell Architecture. ACS Synth. Biol. 7. https://doi.org/10.1021/acssynbio.8b00104

Gureasko, J., Galush, W.J., Boykevisch, S., Sondermann, H., Bar-Sagi, D., Groves, J.T., Kuriyan, J., 2008. Membrane-dependent signal integration by the Ras activator Son of sevenless. Nat. Struct. Mol. Biol. 15. https://doi.org/10.1038/nsmb.1418

Harris, D.C., Jewett, M.C., 2012. Cell-free biology: Exploiting the interface between synthetic biology and synthetic chemistry. Curr. Opin. Biotechnol. https://doi.org/10.1016/j.copbio.2012.02.002

Hong, S., Hong, I., Han, A., Seo, J.Y., Namgung, J., 2015. A new method of artificial latent fingerprint creation using artificial sweat and inkjet printer. Forensic Sci. Int. 257, 403–408. https://doi.org/10.1016/j.forsciint.2015.10.005

Hosseini, S., Vázquez-Villegas, P., Rito-Palomares, M., Martinez-Chapa, S.O., 2018. Enzyme-Linked Immunosorbent Assay (ELISA): From A to Z, Springer Briefs in Applied Sciences and Technology: Forensic and Medical Bioinformatics.

Hui, E., Vale, R.D., 2014. In vitro membrane reconstitution of the T-cell receptor proximal signaling network. Nat. Struct. Mol. Biol. https://doi.org/10.1038/nsmb.2762

Jacot-Descombes, L., Gullo, M.R., Cadarso, V.J., Brugger, J., 2012. Fabrication of epoxy spherical microstructures by controlled drop-on-demand inkjet printing. J. Micromechanics Microengineering 22. https://doi.org/10.1088/0960-1317/22/7/074012

Khodayari Bavil, A., Kim, J., 2018a. A capillary flow-driven microfluidic system for microparticle-labeled immunoassays. Analyst 143, 3335–3342. https://doi.org/10.1039/c8an00898a

Khodayari Bavil, A., Kim, J., 2018b. A capillary flow-driven microfluidic system for microparticle-labeled immunoassays. Analyst 143, 3335–3342. https://doi.org/10.1039/C8AN00898A

Kim, J., Jensen, E.C., Megens, M., Boser, B., Mathies, R.A., 2011. Integrated microfluidic bioprocessor for solid phase capture immunoassays. Lab Chip 11, 3106–3112. https://doi.org/10.1039/c1lc20407f

Kong, F., Yuan, L., Zheng, Y.F., Chen, W., 2012. Automatic liquid handling for life science: A critical review of the current state of the art. J. Lab. Autom. https://doi.org/10.1177/2211068211435302

Lee, B.S., Lee, J.-N., Park, J.-M., Lee, J.-G., Kim, S., Cho, Y.-K., Ko, C., 2009a. A fully automated immunoassay from whole blood on a disc. Lab Chip 9, 1548. https://doi.org/10.1039/b820321k

Lee, B.S., Lee, J.N., Park, J.M., Lee, J.G., Kim, S., Cho, Y.K., Ko, C., 2009b. A fully automated immunoassay from whole blood on a disc. Lab Chip 9, 1548–1555. https://doi.org/10.1039/b820321k

Lequin, R.M., 2005. Enzyme immunoassay (EIA)/enzyme-linked immunosorbent assay (ELISA). Clin. Chem. 51, 2415–2418. https://doi.org/10.1373/clinchem.2005.051532

Leung, K., Zahn, H., Leaver, T., Konwar, K.M., Hanson, N.W., Page, A.P., Lo, C.-C., Chain, P.S., Hallam, S.J., Hansen, C.L., 2012. A programmable droplet-based microfluidic device applied to multiparameter analysis of single microbes and microbial communities. Proc. Natl. Acad. Sci. 109, 7665–7670. https://doi.org/10.1073/pnas.1106752109

Li, B., Fan, J., Li, J., Chu, J., Pan, T., 2015. Piezoelectric-driven droplet impact printing with an interchangeable microfluidic cartridge. Biomicrofluidics. https://doi.org/10.1063/1.4928298

Li, F., You, M., Li, S., Hu, J., Liu, C., Gong, Y., Yang, H., Xu, F., 2020. Paper-based point-of-care immunoassays: Recent advances and emerging trends. Biotechnol. Adv. https://doi.org/10.1016/j.biotechadv.2019.107442

Li, J., Carney, R.P., Liu, R., Fan, J., Zhao, S., Chen, Y., Lam, K.S., Pan, T., 2018a. Microfluidic Print-to-Synthesis Platform for Efficient Preparation and Screening of Combinatorial Peptide Microarrays. Anal. Chem. 90, 5833–5840. https://doi.org/10.1021/acs.analchem.8b00371

Li, J., Tan, W., Xiao, W., Carney, R.P., Men, Y., Li, Y., Quon, G., Ajena, Y., Lam, K.S., Pan, T., 2018b. A Plug-and-Play, Drug-on-Pillar Platform for Combination Drug Screening Implemented by Microfluidic Adaptive Printing. Anal. Chem. https://doi.org/10.1021/acs.analchem.8b03456

Li, J., Zhao, S., Yang, G., Liu, R., Xiao, W., Disano, P., Lam, K.S., Pan, T., 2019. Combinatorial Peptide Microarray Synthesis Based on Microfluidic Impact Printing. ACS Comb. Sci. 21, 6–10. https://doi.org/10.1021/acscombsci.8b00125

Liu, C., Tomizuka, M., 2016. Algorithmic safety measures for intelligent industrial co-robots, in: Proceedings - IEEE International Conference on Robotics and Automation. pp. 3095–3102. https://doi.org/10.1109/ICRA.2016.7487476

Lorenz, M.G.O., 2004. Liquid-Handling Robotic Workstations for Functional Genomics. J. Lab. Autom. 9, 262–267. https://doi.org/10.1016/j.jala.2004.03.010

Mao, Y., Pan, Y., Li, X., Li, B., Chu, J., Pan, T., 2018. High-precision digital droplet pipetting enabled by a plug-and-play microfluidic pipetting chip. Lab Chip 18, 2720–2729. https://doi.org/10.1039/c8lc00505b

Mathes, S.H., Parker, C.N., 2017. Requirements of skin tissue models for high-throughput screening, Skin Tissue Models. Elsevier Inc. https://doi.org/10.1016/B978-0-12-810545-0.00018-8

Mattheakis, L., 2014. Screening robotics and automation. J. Biomol. Screen. 19, 478–480. https://doi.org/10.1177/1087057113517980

Miller, T.E., Beneyton, T., Schwander, T., Diehl, C., Girault, M., McLean, R., Chotel, T., Claus, P., Cortina, N.S., Baret, J.C., Erb, T.J., 2020. Light-powered CO2 fixation in a chloroplast mimic with natural and synthetic parts. Science (80-.). 368. https://doi.org/10.1126/science.aaz6802

Mitchell, H.T., Noxon, I.C., Chaplan, C.A., Carlton, S.J., Liu, C.H., Ganaja, K.A., Martinez, N.W., Immoos, C.E., Costanzo, P.J., Martinez, A.W., 2015. Reagent pencils: A new technique for solvent-free deposition of reagents onto paper-based microfluidic devices. Lab Chip 15, 2213–2220. https://doi.org/10.1039/c5lc00297d

Morris, M.C., 2013. Fluorescent biosensors - Probing protein kinase function in cancer and drug discovery. Biochim. Biophys. Acta - Proteins Proteomics. https://doi.org/10.1016/j.bbapap.2013.01.025

O’Connell, T.N., Ramsay, J., Rieth, S.F., Shapiro, M.J., Stroh, J.G., 2014. Solution-based indirect affinity selection mass spectrometry-A general tool for high-throughput screening of pharmaceutical compound libraries. Anal. Chem. 86, 7413–7420. https://doi.org/10.1021/ac500938y

Oh, W.K., Kim, S., Shin, K.H., Jang, Y., Choi, M., Jang, J., 2013. Inkjet-printed polyaniline patterns for exocytosed molecule detection from live cells. Talanta 105, 333–339. https://doi.org/10.1016/j.talanta.2012.10.050

Oosterbroek, R.E., van den Berg, A., 2003. Lab-on-a-Chip: Miniaturized Systems for (Bio) Chemical Analysis and Synthesis, Lab-on-a-Chip: Miniaturized Systems for (Bio) Chemical Analysis and Synthesis. https://doi.org/10.1016/B978-0-444-51100-3.X5000-1

Peeling, R.W., Holmes, K.K., Mabey, D., Ronald, A., 2006. Rapid tests for sexually transmitted infections (STIs): The way forward. Sex. Transm. Infect. https://doi.org/10.1136/sti.2006.024265

Rane, T.D., Zec, H.C., Wang, T.H., 2015. A barcode-free combinatorial screening platform for matrix metalloproteinase screening. Anal. Chem. 87. https://doi.org/10.1021/ac504330x

Reis, N., Ainsley, C., Derby, B., 2005. Ink-jet delivery of particle suspensions by piezoelectric droplet ejectors. J. Appl. Phys. 97. https://doi.org/10.1063/1.1888026

Sanjay, S.T., Li, M., Zhou, W., Li, Xiaochun, Li, XiuJun, 2020. A reusable PMMA/paper hybrid plug-and-play microfluidic device for an ultrasensitive immunoassay with a wide dynamic range. Microsystems Nanoeng. 6, 28. https://doi.org/10.1038/s41378-020-0143-5

Scott-brown, J., Papachristodoulou, A., 2017. Visual Representation of Experimental Protocols 1–10.

Setti, L., Fraleoni-Morgera, A., Ballarin, B., Filippini, A., Frascaro, D., Piana, C., 2005. An amperometric glucose biosensor prototype fabricated by thermal inkjet printing, in: Biosensors and Bioelectronics. pp. 2019–2026. https://doi.org/10.1016/j.bios.2004.09.022

Shim, J., Zhou, C., Gong, T., Iserlis, D.A., Linjawi, H.A., Wong, M., Pan, T., Tan, C., 2021. Building protein networks in synthetic systems from the bottom-up. Biotechnol. Adv.

https://doi.org/10.1016/j.biotechadv.2021.107753

Sirringhaus, H., Kawase, T., Friend, R.H., Shimoda, T., Inbasekaran, M., Wu, W., Woo, E.P., 2000. High-resolution inkjet printing of all-polymer transistor circuits. Science (80-.). 290, 2123–2126. https://doi.org/10.1126/science.290.5499.2123

Smith, C., 2007. Tools for drug discovery: Tools of the trade. Nature. https://doi.org/10.1038/446219a

Song, Y., Wang, Y., Qi, W., Li, Y., Xuan, J., Wang, P., Qin, L., 2016. Integrative volumetric bar-chart chip for rapid and quantitative point-of-care detection of myocardial infarction biomarkers. Lab Chip 16. https://doi.org/10.1039/c6lc00561f

Su, X., Ditlev, J.A., Hui, E., Xing, W., Banjade, S., Okrut, J., King, D.S., Taunton, J., Rosen, M.K., Vale, R.D., 2016. Phase separation of signaling molecules promotes T cell receptor signal transduction. Science (80-.). https://doi.org/10.1126/science.aad9964

Villarreal, F., Contreras-Llano, L.E., Chavez, M., Ding, Y., Fan, J., Pan, T., Tan, C., Contreras-Llano, L.E., Chavez, M., Tan, C., 2018. Synthetic microbial consortia enable rapid assembly of pure translation machinery. Nat. Chem. Biol. 14, 29–35. https://doi.org/10.1038/nchembio.2514

Villarreal, F., Tan, C., 2017. Cell-free systems in the new age of synthetic biology. Front. Chem. Sci. Eng. https://doi.org/10.1007/s11705-017-1610-x

Vinet, L., Zhedanov, A., 2011. A “missing” family of classical orthogonal polynomials, Journal of Physics A: Mathematical and Theoretical. https://doi.org/10.1088/1751-8113/44/8/085201

Wang, D., Gou, S.Y., Axelrod, D., 1992. Reaction rate enhancement by surface diffusion of adsorbates. Biophys. Chem. 43. https://doi.org/10.1016/0301-4622(92)80027-3

Wang, J., Deng, K., Zhou, C., Fang, Z., Meyer, C., Deshpande, K.U.A., Li, Z., Mi, X., Luo, Q., Hammock, B.D., Tan, C., Chen, Y., Pan, T., 2019. Microfluidic cap-To-dispense (μCD): A universal microfluidic-robotic interface for automated pipette-free high-precision liquid handling. Lab Chip 19, 3405–3415. https://doi.org/10.1039/c9lc00622b

Weiss, M., Frohnmayer, J.P., Benk, L.T., Haller, B., Janiesch, J.W., Heitkamp, T., Börsch, M., Lira, R.B., Dimova, R., Lipowsky, R., Bodenschatz, E., Baret, J.C., Vidakovic-Koch, T., Sundmacher, K., Platzman, I., Spatz, J.P., 2018. Sequential bottom-up assembly of mechanically stabilized synthetic cells by microfluidics. Nat. Mater. https://doi.org/10.1038/NMAT5005

Yang, M., Sun, S., Kostov, Y., Rasooly, A., 2011. An automated point-of-care system for immunodetection of staphylococcal enterotoxin B. Anal. Biochem. 416, 74–81. https://doi.org/10.1016/j.ab.2011.05.014

Yoshioka, Y., Jabbour, G.E., 2006. Desktop inkjet printer as a tool to print conducting polymers. Synth. Met. 156, 779–783. https://doi.org/10.1016/j.synthmet.2006.03.013

Yuen, P.K., Goral, V.N., 2010. Low-cost rapid prototyping of flexible microfluidic devices using a desktop digital craft cutter. Lab Chip 10. https://doi.org/10.1039/b918089c

Zakir Hossain, S.M., Luckham, R.E., Smith, A.M., Lebert, J.M., Davies, L.M., Pelton, R.H., Filipe, C.D.M., Brennan, J.D., 2009. Development of a bioactive paper sensor for detection of neurotoxins using piezoelectric inkjet printing of sol-gel-derived bioinks. Anal. Chem. 81, 5474–5483.

https://doi.org/10.1021/ac900660p

Zhang, K., Gao, M., Chong, Z., Li, Y., Han, X., Chen, R., Qin, L., 2016. Single-cell isolation by a modular single-cell pipette for RNA-sequencing. Lab Chip 16, 4742–4748. https://doi.org/10.1039/c6lc01241h

Zhao, C., Si, Y., Pan, B., Taha, A.Y., Pan, T., Sun, G., 2020. Design and fabrication of a highly sensitive and naked-eye distinguishable colorimetric biosensor for chloramphenicol detection by using ELISA on nanofibrous membranes. Talanta 217. https://doi.org/10.1016/j.talanta.2020.121054

Zheng, C., Wang, Jingwen, Pang, Y., Wang, Jianbin, Li, W., Ge, Z., Huang, Y., 2012. High-throughput immunoassay through in-channel microfluidic patterning. Lab Chip 12, 2487–2490. https://doi.org/10.1039/c2lc40145b

Chapter 2 RoMI for automated pipette-free high-precision liquid handling

2.1 Abstract

Microfluidic devices have been increasingly used for low-volume liquid handling operations. However, laboratory automation of such delicate devices has lagged behind due to the lack of world-to-chip (macro-to-micro) interfaces. In this chapter, we have presented the first pipette-free robotic-microfluidic interface using a microfluidic-embedded container cap, referred to as a Microfluidic Cap-to-Dispense (μCD), to achieve a seamless integration of liquid handling and robotic automation without any traditional pipetting steps. The μCD liquid handling platform offers a generic and modular way to connect the robotic device to standard liquid containers. It utilizes the high accuracy and high flexibility of the robotic system to recognize, capture and position; and then using microfluidic adaptive printing it can achieve high-precision on-demand volume distribution. With its modular connectivity, nanoliter processability, high adaptability, and multitask capacity, μCD shows great potential as a generic robotic-microfluidic interface for complete pipette-free liquid handling automation.

2.2 Working Principle

The μCD system is designed to establish a universal interface between robotic automation and liquid handling of chemical and biological solutions without involvement of traditional micropipetting processes.(Kong et al., 2012) It comprises of four essential components: the microfluidic dispensing cap, the robotic end-effector with pneumatic connectors, the robotic arm/motion stage, and a machine vision unit for recognition, as shown in Fig. 2-1a.

As the key component, the microfluidic dispensing cap has been fabricated by stacking three polymer layers from bottom to top, as shown in Fig. 2-1b: a membrane layer with a high-precision micro-machined nozzle, a microfluidic channel layer, and a 3D-printed fitting adapter. The micro-machined nozzle plays an important role in determining the process for droplet pinch-off and ejection, while the microfluidic layer balances the discrete output of droplets and constantly refills the fluid. Moreover, the custom 3D-printed adapter is intended to fit and connect to standard liquid containers with various sizes in a regular lab setting, but also incorporates all liquid and pneumatic connections, such as a channel towards the microfluidic layer, another tube connected to the enclosed solution, along with two additional pneumatic channels that can be reversibly linked to the robotic end-effector upon contact.

Notably, the classic robotic end-effector, a parallel-styled gripper with two fingers, is equipped with a rubber contact pad on each finger to catch the microfluidic dispensing cap with the pneumatic channels, as illustrated in Fig. 2-1a. The elastic pads made of rubber resin have been embedded in the pneumatic connections using O-ring seals. Upon contact, the compressed air from the programmable pneumatic drive can be directed towards the microfluidic dispensing cap to refill and dispense the droplets from different channels with a millisecond resolution. A 4 degree-of-freedom robotic arm has been combined with the end-effector to enable automated manipulations. An expanded IO on the robotic arm has been utilized as a communication means to coordinate and synchronize the functions, such as movement, catch-and-release, and dispensing.

The machine vision module achieves two functions. The first is to recognize the container information encoded by a QR code on the side of the cap, and the second is to use the QR code as reference coordinates and to help position the dispensing cap for further operations. Specifically, when guided by the machine vision, the robotic arm first identifies and locates the container with the targeted reagent using the QR code. Consecutively, the end-effector (gripper) is commanded to engage into the two opposite sides of the microfluidic cap with pneumatic connections established.

As depicted in Fig. 2-1c, the droplet printing process is controlled and propelled by two external pneumatic drives: a low-pressure source (P_L) to load the liquid from the container to the dispensing nozzle and a pulsed high-pressure one (P_H) to eject droplets from the nozzle. Fig. 2-1d illustrate simplified hydraulic circuits to describe the two states of the droplet dispensing process labeled with major influential parameters, namely a loading/refilling state (top) and a dispensing state (bottom). In particular, the fluid dynamics inside the microchannel can be modeled as a constant displaced flow caused by the continuous input of refilling liquid and the dispensing output of discrete droplet volumes. The displaced flow moves through the microchannel, with flow resistance of Rc, towards either the nozzle openings with flow resistance of Rn or the adjacent side channel with flow resistance of Rr. At the interface between the side channel and the robotic effector, a one-way valve is attached to prevent the fluid from leaking into the pneumatic drive.

During the refilling state, liquid from the container will fill out the microfluidic cap while stopping at the dispensing nozzle and the robotic interface with the one-way valve, both of which can be modelled as fluidic diodes Dn and Dr, respectively, as shown in Fig. 2-1d. As the refilling pressure P_L is smaller than either the valve-opening pressure or the Laplace pressure of the nozzle, the liquid will reach an equilibrium state after filling up the dispensing cap. Once a high pulse pressure P_H is applied from the side channel during the subsequent printing state, a droplet with a volume of V is ejected through the nozzle opening with a volumetric flowrate of Q. The following equation expresses the relationship between the dispensed droplet volume (V) and the flow resistance of the microfluidic channel and the nozzle opening along with the pneumatic drives:

$$V = Q \cdot T = \frac{P_H/R_r + P_L/R_c}{1/R_r + 1/R_n + 1/R_c} \cdot \frac{T}{R_n} \approx \frac{P_H \cdot T}{R_n} = \frac{P_H \cdot T \cdot \pi r^4}{8\mu t} \qquad \textit{(Eq. 1)}$$

where T is the duration of the pulsed pressure, r is the nozzle radius, t is the nozzle thickness and μ is the dynamic viscosity of the liquid. Notably, in the dispensing cap design, we apply a design rule to keep *Rr* << *Rn* << *Rc*, which further simplifies the equation. Within the laminar flow region, the flow resistance of the nozzle Rn follows the classic Hagen-Poiseuille equation (Sutera and Skalak, 1993). It is also worth noting that the hydrostatic pressure from the liquid height is considerably smaller than the refilling pressure, and therefore, it has been neglected in the equation.

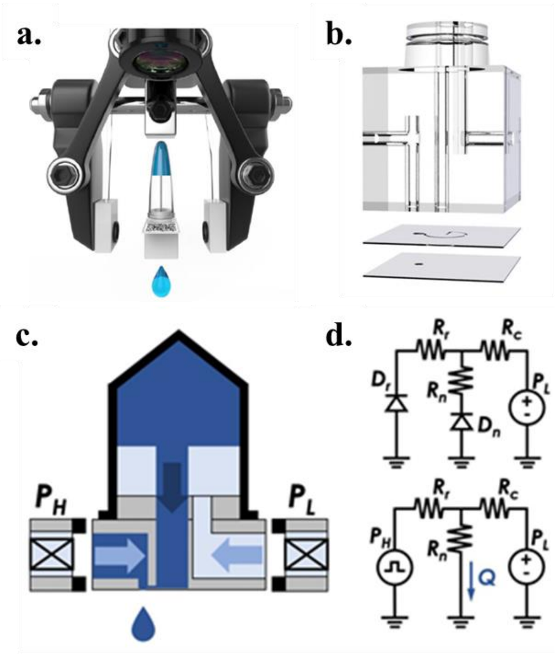

Fig. 2-1 Illustrations of a) 3D illustration of the microfluidic-robotic interface (MRI); b) 3D illustration of the microfluidic-embedded cap dispenser; c-d) Hydraulic circuits for describing the two states of the droplet dispensing process labeled with major influential parameters, namely a refilling state and a printing state.

2.3 Materials and Methods

2.3.1 Design and fabrication of the microfluidic cap

A UV-laser (JG15S, Zhengye Laser, China) was used to ablate a PMMA membrane to form nozzles. The laser ablation parameters were optimized to achieve a uniform edge of the circular though hole, resulting in a vertical pinch-off process for droplet generation with rare satellites scattering on the substrates and rare droplets adhering to the nozzles. Micro-circles with radius of 5, 15, 25, 35, 45 and 55 µm were designed using CAD software and produced ablated nozzles with radius of 25, 32.5, 40, 50, 62.5, and 75 µm, by shrinking the PMMA material (thickness: 75 µm) at a high temperature. The UV-laser was also used to ablate a double-side membrane (ARcare® 90445, Adhesives Research, thickness of 80 µm) to form microchannels with a width of about 800 µm. The milli-chip was designed in SolidWorks software and fabricated with a photosensitive resin using a 3D printer (Shenzhen WeNext Technology Co., Ltd), with 1 mm-diameter inlets and outlets.

The micro-chip layer was stuck onto the top of the milli-chip, with channel endings aligned to the two openings on the bottom surface of milli-chip for liquid refilling and output, respectively. The nozzle layer was then stuck onto the microchip, with nozzle aligned to the end of the microchannel for liquid dispensing. Subsequently, a steel needle (1 mm diameter, 1.2 cm length) was inserted into the center hole of the plug part of the milli-chip. Then the whole fabricated microfluidic caps were fabricated to fit by insertion into standard liquid containers, such as 200 µL EP tubes.

There are three round through-holes (diameter: 1 mm) in the milli-chip for the gas and liquid drive: one side-through-hole with 90-degree bend upward for transfer compressed air to drive the liquid in the the container into the steel needle; then liquid goes though the steel needle and center-through-hole to fill liquid into the micro-chip. Liquid flows through the nozzle and upward to another side-through-hole with 90-degree bend and stops at the one-way valve. Pneumatic pulse pressure then goes through the valve and pushes the liquid toward the microchannel and nozzle, as shown in Fig. 2-1c.

The nozzle and microchannel were designed to have a high resistance for precise droplet volume control. After the droplets are pinched off under the nozzle, the residual liquid is retracted backwards into the microchannel, driven by its Laplace pressure (Derby, 2010), while the microchannel balances the discrete output of droplets and constantly refills the liquid. The displaced flow moves through the microchannel either upwards to the pulse source or downwards to the nozzle. When the pulsed air pressure is switched on and off, the extra volume of fluid is ejected through the nozzle opening, not backward into the microchannel due to its high resistance $Rc >> Rn$.

2.3.2 Calibration and imaging methods

Planar PDMS membranes coated on glass-slide substrates were used as the calibration surface to characterize the volumes of the printed aqueous droplets. Since the contact angle of bare PDMS is close to 90 degrees, it offered a simple method to calculate the volume of these hemispherical droplets. To decrease the evaporation rate, dimethylsulfoxide (DMSO) was added to the aqueous solution with a mixing ratio of 2.5: 23.75: 73.75%, color dye: DMSO: deionized water. The images of droplet dispensing process are imaged by a high-speed camera (VEO-E310L, Phantom, USA). To characterize the dispensing parameters, arrays or patterns of droplets were deposited onto the PDMS surface. The images of the droplets were captured with a standard optical microscope (EVOS XL, Life Technologies, USA) and analyzed using the ImageJ software.

2.3.3 System integration and patterning algorithm

To introduce a pneumatic drive into the microfluidic dispensing cap, a robotic end-effector, more specifically, a parallel gripper with two fingers, applies a horizontal force to tightly hold the cap. A pair of customized 3D-printed air connectors with holes in the center surrounded by silica rubber O-rings with a diameter of 2 mm, were mounted on both gripper fingers to introduce compressed air into the cap and guarantee a seamless pneumatic connection as a plug-and-play interface. The compressed air from the programmable pneumatic drive can be precisely controlled and actuated into the two opposite sides of microfluidic cap for accurate refilling and dispensing with sub-millisecond resolution, resulting in the formation of nanoliter droplets. In the pneumatic system, we have included a custom-made circuit based on Arduino architecture and two mini solenoid valves (LHDA1221111H, Lee Co). The pressure pulses have been derived from a pressure regulator (OBKZN) with a range up to 15 psi and a precision of 0.01 psi connected to the compressed air from an air compressor.

To precisely position the droplet in the right place, translational motions were needed for the dispensing task, usually described in a Cartesian coordinate system. A 4-DoF robotic arm was used to achieve this demand, in which three DoFs on the base, the upper arm and the lower arm were programmed to approach the target position in XYZ coordinate system and the last wrist rotational DoF was used to adjust the orientation (of the cap) around the Z-axis.

The robotic end-effector and the arm were combined to form a manipulator, whose functions were coordinated and synchronized with the other parts of the system via the expanded IOs on 5 V TTL-level and 3.3 V LVTTL-level as communication means.

The desired complicated patterns were designed in advance as pixel matrices. On each pixel, the type of the reagent and the droplet count were designated. For each reagent, there will be a matrix, where the value of each element, a natural number, specifies the droplet count. The droplet count can vary from zero to several tens, resulting in a blank spot at a distinct drop. After catching a target reagent from the designated position, the robotic manipulator will move and stay at the printing region and execute the printing task instructed by the corresponding pattern matrix. The stay period was also determined by the droplet count in this position. By providing multiple reagents and their pattern matrices, objects can be mixed in each specified position. The spatial interval of the droplets between the adjacent elements in the pattern matrix was adjustable in the program of the robotic manipulator. Often, the interval was set above 0.5 mm to prevent contamination from adjacent droplets. The presented system enables automated precise dispensing of liquid and reagents in modern complex lab dispensing tasks, such as large-scale complicated pattern in multi-well plates.

2.3.4 Biomolecular micropatterns demonstrations

To demonstrate the compatibility of the µCD system with biological samples a multiparametric dose response experiment was conducted. This experiment consisted of 3 components: bacteria, isopropyl β-D-1-thiogalactopyranoside (IPTG), and Luria Broth (LB). The bacterial strain used in this paper was generated by cloning the fluorescent protein mCherry into the pET15b plasmid and transforming it into *E. coli* BL21 (DE3)-pLysS cells (Novagen). Overnight cultures were made from fresh colonies of that strain. The cultures were then diluted in fresh media 2 hours prior to printing allowing them to reach a concentration of approximately 108 cells/mL. All the reagents were then sequentially printed to build each unique reaction.

The droplets were dispensed onto PDMS-coated cover glass to allow for observation on a Nikon Eclipse Ti-E inverted microscope. A 2 mm-thick layer of mineral oil was added after printing to cover the droplets to avoid evaporation. A Texas red filter cube (560 nm excitation/630 nm emission) from Nikon was used to measure the mCherry fluorescence. Images of the droplets were automatically taken over several hours. The fluorescence intensities in the images were then analyzed using ImageJ and Matlab scripts. The half maximum effective concentration was calculated by determining the inducer concentration required to achieve half the maximal fluorescence for each cell density and then averaged.

2.4 Results and Discussion

2.4.1 Automation of the µCD platform

A complete µCD operation flow includes multistep automation, i.e., sample recognition, catch, positioning, dispensing, return and release, as illustrated in Fig. 2-2. As aforementioned, the target identification has been achieved through the machine vision using a QR-code recognition algorithm (Fig. 2-2a). In addition, the QR-code recognition has provided the robotic arm with spatial coordinates to allocate and capture the targeted containers. The robotic gripper with two fingers grabs the microfluidic dispensing cap with the pneumatic link established (Fig. 2-2b). Following the container capture, the robotic arm moves the c-equipped container to the target position and starts to dispense the liquid driven by the programmed pneumatic control (Fig. 2-2c). After delivering the desired volume, the robot returns the container back to the original location (Fig. 2-2d), while it is ready to start another cycle of dispensing.

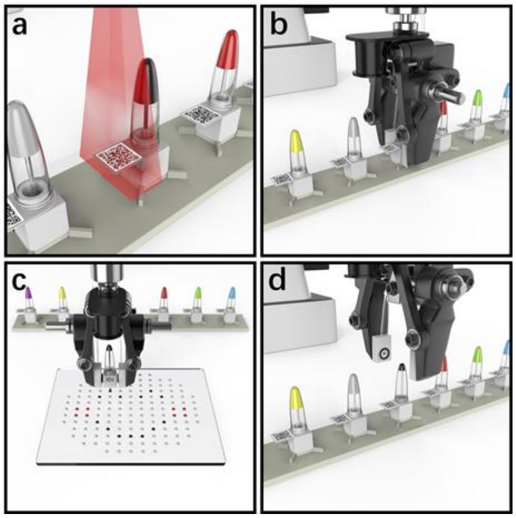

Fig. 2-2 Illustration of the complete μCD operation: a) sample recognition; b) catch and positioning; c) dispensing; and d) return and release.

2.4.2 Characterization of droplet dispensing

The process of droplet formation was recorded using a high-speed camera. As shown in Fig. 2-3, the droplet has immediately emerged from the nozzle from the last ejection (t = 0.1ms); Within a short duration, the droplet tends to move away from the nozzle, forming a characteristic pendent shape (t = 0.6ms); At a critical distance, the liquid bridge would break off and the droplet completely departs from the nozzle (t = 0.8ms); As the droplet further moves, it gradually evolves into a nearly spherical shape with gravitational and inertial influences negligible under its dimensions, while the residue fluid retracts back into the nozzle (t = 1.5ms); Finally, the residue fluid completely returns to the nozzle surface and is ready for the next cycle of droplet ejection (t = 3.5ms).

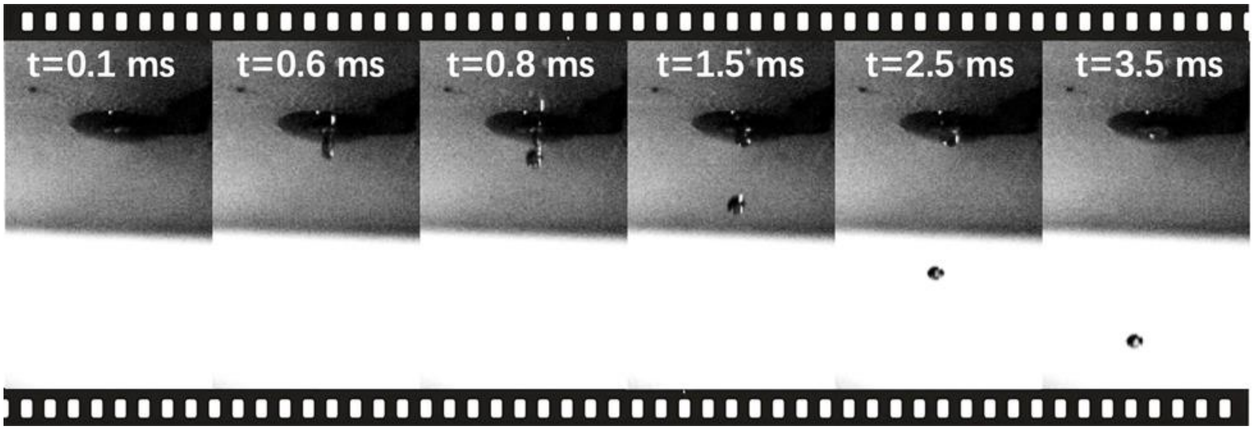

Fig. 2-3 Stroboscopic images showing droplet formation.

The Coefficients of Variation (CVs) have been considered to evaluate the consistency and distribution of the single droplet volumes printed from the µCD system. Fig. 2-4a shows a microscopic image of a printed droplet array on a planar surface from a 25% DMSO solution (with a viscosity of 1.5 cP and surface tension of 55.4 mN/m at 25 ℃) (Lebel and Goring, 1962; Markarian and Terzyan, 2007). Furthermore, the printed single droplet array with the targeted volume of 84 nL have been measured and plotted in Fig. 2-4b. Computed from the droplet diameter measured by the histogram plotted by ImageJ, it shows a mean value of 84 nl and a diameter CV of 3.18%, confirming the high repeatability of the single droplet printing of the µCD system. Furthermore, the linearity of the printed droplet sequences has then been evaluated by repetitive dispensing of 100 to 1000 times, with the single droplet volume targeted at 100 nL. The weights of these printed volumes have been assessed by a high-precision scale and summarized in Fig. 2-4c, where the x-axis represents the targeted volumes while the y-axis stands for the corresponding volumes measured by the gravitational method. As can be seen, the measurement results, based on three-time repeats, have been plotted and fitted into a linear curve, exhibiting a high correlation coefficient of R^2 =0.9994.

For a classic EP tube with capacity of 200 µl, the current µCD design could continuously produce more than 3000 droplets with each loading with 80 µm nozzles, or 9000 droplets with 65 µm nozzles, till the last drop of reagent in the container. This could be highly desirable for the precious biological/chemical reagents. The customized pattern of such has been automated by the robotic arm, by which the positioning precision and spatial resolution are mainly determined.

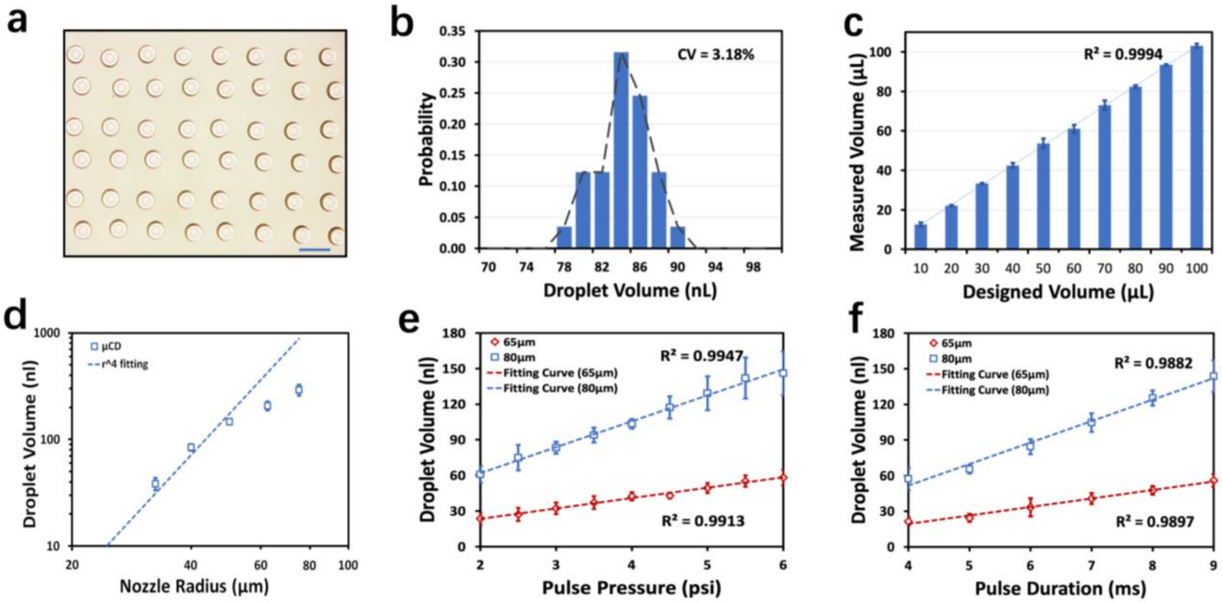

Fig. 2-4 a) The microscopic image of droplets array; Scale bar: 1mm; b) The volume distribution of the array; c) Linearity of accumulated droplets from 100 nl to 1000 nl, with a R2> 0.99; d) The experimental measurements of the ejected droplet volumes depending on multiple nozzle radius, and e) pressure levels, f) pulse durations. In e) and f), the mean droplet volumes are shown in red dots (32.5 µm) and blue dots (40 µm), and all the fitting curves has a R2 > 0.98.

As expressed in Eq. 1 of the microfluidic printing model, a number of potential parameters can influence the droplet formation process, including nozzle radius and thickness, fluidic viscosity, pulse pressure and duration (Choi and Kim, 2016; Li et al., 2018). In this study, we have chosen the major influences of the nozzle radius (r), the pneumatic pressure (P_H) and the pulse duration (T) to be experimentally assessed.

First of all, the nozzle dimension (r) plays an important role in determining the droplet volume (Ding et al., 2013). A range of different nozzle radius with the same milli- and micro-chips have been investigated with the droplet variations in response to the driving pulses. As shown in Fig. 2-4d, given a fixed pulse pressure of 3.0 psi and pulse duration of 6 ms, the ejected droplet volume increases in an approximately linear fashion from 38 nL to 291 nL with the nozzle radius rising from 32.5 to 75 µm, that is 7-fold volume expansion. As expected, when the nozzle size keeps small, the experimental data match well with the inverse 4th-power relationship between the droplet volume and nozzle dimension, as can be theoretically predicted by Eq. 1. However, as the nozzle size increases (above 60 µm in radius), the original assumption of $Rr << Rn$ becomes no longer valid, and therefore, the experimentally measured values deviate from the theoretical predication of the desired droplet volume by a large margin. These deviations become more severe in a larger nozzle as shown experimentally.

Further reducing the nozzle dimension would result in drastic decrease in the droplet size; meanwhile, it causes the nozzle resistance to hike considerably. However, to eject the fluid out from the nozzle using the MAP principle, it requires the nozzle resistance *Rn* to be considerably lower than that of the microchannels *Rc*. We have experimentally determined that the minimal nozzle radius would be greater than 25 µm for effective printing in the µCD platform. On the other hand, a wider nozzle would lead to larger ejected droplets, while the maximal refilling speed of the liquid sample is directly proportional to the microchannel resistance, and caped at about 300 nL/s in the system, given the refilling pressure of 0.5 psi and pulse duration of 20 ms.

Besides the nozzle geometry, the pneumatic drive pressure (P_H) can also be determinant in the droplet formation, as the model predicts (Fig. 2-1c). We have investigated the influences from the magnitude and pulse duration of the pneumatic drive, respectively. Fig. 2-4e illustrates the experimental results of the droplet volumes at multiple pressure levels, given a fixed pulse duration. As evident by a well-fitted measurement curve, the rising volume of the ejected droplets is nearly linearly correlated with the elevating pulse pressure. In particular, by extending the pneumatic pressure from 2.0 psi to 6.0 psi, the droplet size has been scaled with more than 2-fold increment from 23 to 58 nL with 32.5 µm nozzles, and 60 to 145 nL with 40 µm nozzles, at the fixed pulse duration (of 6 ms). It is worth noting that a minimal pressure (of 2.0 psi) becomes necessary to overcome both the internal resistance of the microchannels and Laplace pressure presented at the nozzle for the droplet formation (Brian Derby, 2010). Moreover, Fig. 2-4f shows a similar linear relationship between the pulse duration and the droplet volume, ranging from 21 to 55 nL with 32.5 µm nozzles, and 57 to 143 nL with 40 µm nozzles, at the fixed pulse pressure (of 3.0 psi). In principle, a shorter pulse duration would lead to faster droplet ejections, and thus, a higher dispensing speed. However, the restrictions have been presented by both the mechanical response time of the solenoid valve (~2 ms) and the response time of the compressed air pressure inside the channel, from which a minimal pulse duration of 3 ms is resulted. In conclusion, the droplet sizes can be fine-tuned by either the geometrical parameter of the nozzle (i.e., its radius) or the on-demand pneumatic drive pressure (i.e., the pressure level and duration).

2.4.3 Demonstrations of the µCD platform

As discussed above, the µCD dispensing platform would enable the complete lab automation solution with high throughput and low reagent consumption for various biological and clinical procedures. As proof-of-concept experiments, we have established collective patterns of monochrome or multi-colored droplets to images of combinational arrays, as shown in Fig. 2-5. It includes a planar molecular pattern with single and multiple droplet dispensing (Fig. 2-5a); a Taiji pattern (Fig. 2-5b) and an Eiffel tower shape (Fig. 2-5c) with two different colors printed from separate µCD containers; a multicolor DNA helix structure, with strangled chains presented by two types of 5-in-1 droplets (red and light blue dots) and A/T/C/G by multicolor single droplets (pink, green, yellow and purple), respectively (Fig. 2-5d); a world map formed by an array of 985 single droplets (Fig. 2-5e); and a multicolor droplet array to form logos of the UC DAVIS and SIAT CAS (Fig. 2-5f). The multiplexed and combinatorial pattern formation illustrates the automated multi-reagent processing. As each dispensing, µCD container with caps is independent and modularized, the entire robotic operating system can be easily expanded to large-scale multi-reagents dispensing applications, without a limited number of reagents.

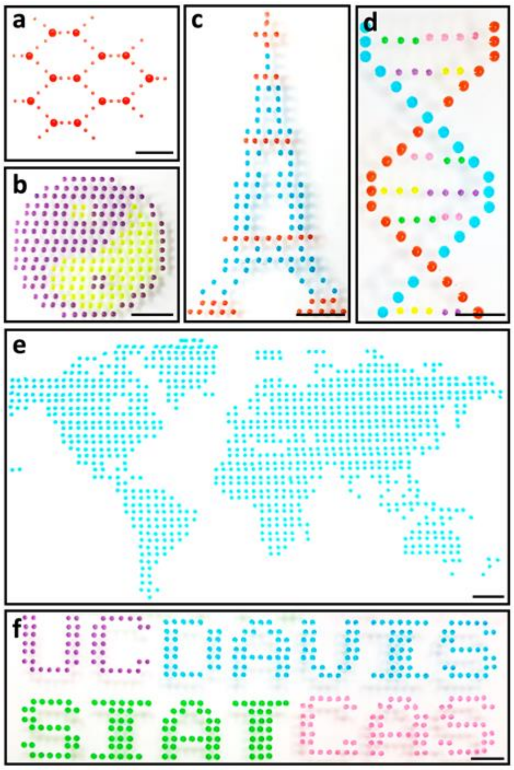

Fig. 2-5 Monochrome or multi-colored Droplets-based patterns: a) molecular; b) Taiji; c) Eiffel tower; d) DNA helix; e) world map; and f) UC-DAVIS and SIAT-CAS logos. (scale bar: 5 mm)

To demonstrate the compatibility of the μCD system with biological sample processing, we implemented a generic combinatorial experiment utilizing three different reagents to assess their interactions. The components included a strain of bacteria with an inducible genetic circuit, an inducer, and a diluent. The objective of this experiment was to characterize the response of the genetic circuit at various concentrations against a range of inducer concentrations. Such experiments are required when constructing complex genetic systems (Zong et al., 2018), assessing the efficacy of a drug on a system (Ding et al., 2015), and optimizing component stoichiometry in a variety of reactions (Fan et al., 2017).

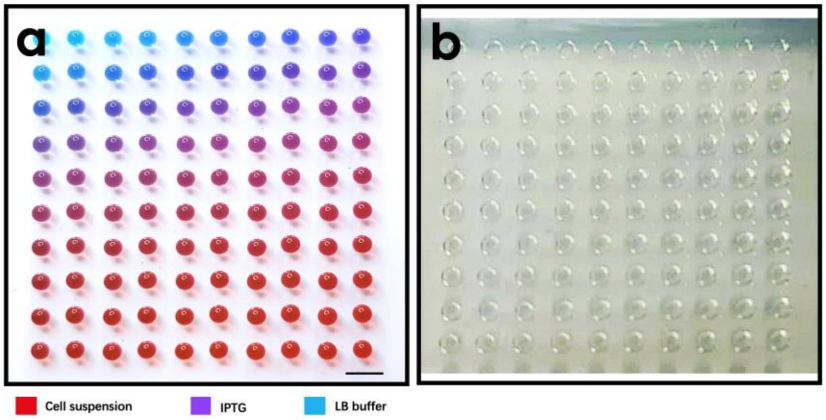

Fig. 2-6 Photos of the 10 x10 array of combinatorial mixtures comprised of a)3 color dyes， with red representative of cell suspension, purple of IPTG, and blue of LB buffer; and b) biological samples of cell suspension, IPTG, and LB buffer.

Here, we studied the response of a LacI repressible genetic circuit, which would give rise to the expression of the fluorescent protein mCherry upon sufficient induction by its inducer, isopropyl β-D-1-thiogalactopyranoside (IPTG). To achieve this, a 10-fold range of concentrations of both the bacteria and the inducer were tested in one hundred independent reaction conditions in which each spot contained 18 ejections, leading to 1.2 μL in total. To ensure the dispensing accuracy of the proposed biological experiment, a 10 x10 array of combinatorial mixtures comprised of 3 color dyes were first generated using the µCD system as shown in Fig. 2-6a, followed by the dispensing the biological samples and reagents, as shown in Fig. 2-6b.

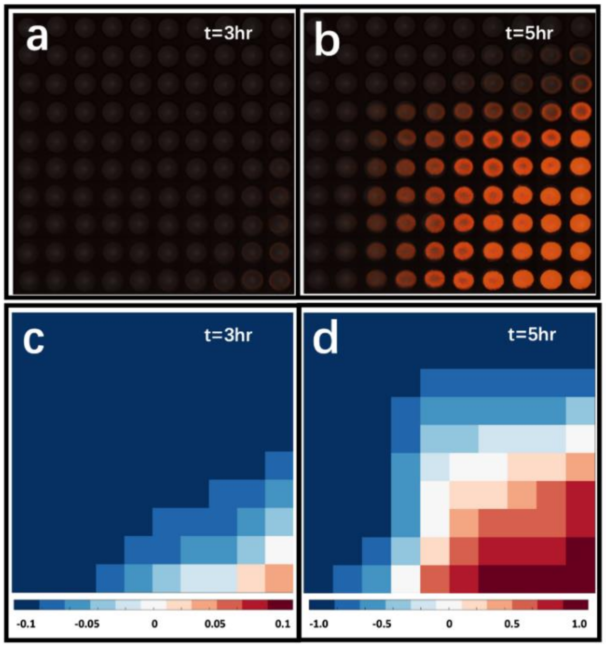

Fig. 2-7 The Response of a LacI repressible genetic circuit. a) 3-hr and b) 5-hr results merged by bright field and fluorescent imaging results from the combinatorial droplet array with cell suspension, IPTG, and LB buffer; c) 3-hr and d) 5-hr heat maps analyzed from fluorescent images.

As a result, the two-dimensional combinatorial matrix of the cell suspension and inducer assay was established. Fig. 2-7a and b show the fluorescent images taken from the combinatorial droplet array, at 3 and 5 hours, respectively. To quantify these images, the total fluorescent densities were measured and normalized in the range -1 to 1 as shown in Fig. 2-7c and d. with ranges of [-0.1, 0.1] and [-1, 1] respectively. From this data, we determined the half maximal effective concentration (EC50) of IPTG to activate the circuit to be around 66.7 µM. The EC¬50¬ determined by this experiment is consistent with previously reported characterizations of similar genetic circuits (Baneyx, 1999; Gardner et al., 2000). This experiment also demonstrates printing of sensitive reagents, which if exposed to harsh conditions will cease to work. The µCD also demonstrates its ability to limit cross contamination between reagents as no fluorescence is observed in droplets without cells or inducer. Compared with the manual dilution processes operated in many biological labs, our μCD system offers a fully automated pipette-free solution with considerable improvement in efficiency and accuracy of multifactorial studies, while completely liberating laboratory personnel from repetitive and routine pipetting work with human-induced errors and interventions eliminated.

2.5 Conclusions

In this chapter, we have developed a pipette-free microfluidic cap-to-dispense method, employing a microfluidic cap with seamless plug-and-play connectivity to robots. It allows automatic high-precision sample dispensing ranging from nano-liter to micro-liter volumes, directly from standard biological containers, without involving any pipetting transfer and potential cross-contamination procedure. As a paradigm-shifting platform, this μCD robotic liquid handling system offers several distinct features, compared to existing liquid handling technologies, including: 1) a fully-automated robotic interface; 2) highly-precise tunable microfluidic dispensing; 3) multi-task operations, including recognizing, capture, positioning, dispensing and releasing; 4) a broad applicability and flexibility for a wide range of biological operations; 5) sample storage in containers with reusable μCD caps for rare or expensive samples. Moreover, the microfluidic cap is ready for mass-production-ready and serves as an inexpensive and disposable platform for various research and development applications.

References

Baneyx, F., 1999. Recombinant protein expression in *Escherichia coli*. Curr. Opin. Biotechnol. https://doi.org/10.1016/S0958-1669(99)00003-8

Brian Derby, 2010. Inkjet printing of functional and structural materials: Fluid property requirements, feature stability, and resolution. Annu. Rev. Mater. Res. https://doi.org/10.1146/annurev-matsci-070909-104502

Choi, I.H., Kim, J., 2016. A pneumatically driven inkjet printing system for highly viscous microdroplet formation. Micro Nano Syst. Lett. 4. https://doi.org/10.1186/s40486-016-0030-x

Derby, B., 2010. Inkjet Printing of Functional and Structural Materials: Fluid Property Requirements, Feature Stability, and Resolution. Annu. Rev. Mater. Res. 40, 395–414. https://doi.org/10.1146/annurev-matsci-070909-104502

Ding, Y., Huang, E., Lam, K.S., Pan, T., 2013. Microfluidic impact printer with interchangeable cartridges for versatile non-contact multiplexed micropatterning. Lab Chip 13, 1902–1910. https://doi.org/10.1039/c3lc41372a

Ding, Y., Li, J., Xiao, W., Xiao, K., Lee, J., Bhardwaj, U., Zhu, Z., Digiglio, P., Yang, G., Lam, K.S., Pan, T., 2015. Microfluidic-Enabled Print-to-Screen Platform for High-Throughput Screening of Combinatorial Chemotherapy. Anal. Chem. 87, 10166–10171. https://doi.org/10.1021/acs.analchem.5b00826

Fan, J., Villarreal, F., Weyers, B., Ding, Y., Tseng, K.H., Li, J., Li, B., Tan, C., Pan, T., 2017. Multi-dimensional studies of synthetic genetic promoters enabled by microfluidic impact printing. Lab Chip 17, 2198–2207. https://doi.org/10.1039/c7lc00382j

Gardner, T.S., Cantor, C.R., Collins, J.J., 2000. Construction of a genetic toggle switch in *Escherichia coli*. Nature 403, 339–342. https://doi.org/10.1038/35002131

Kong, F., Yuan, L., Zheng, Y.F., Chen, W., 2012. Automatic liquid handling for life science: A critical review of the current state of the art. J. Lab. Autom. https://doi.org/10.1177/2211068211435302

Lebel, R.G., Goring, D.A.I., 1962. Density, Viscosity, Refractive Index, and Hygroscopicity of Mixtures of Water and Dimethyl Sulfoxide. J. Chem. Eng. Data 7, 100–101. https://doi.org/10.1021/je60012a032

Li, J., Carney, R.P., Liu, R., Fan, J., Zhao, S., Chen, Y., Lam, K.S., Pan, T., 2018. Microfluidic Print-to-Synthesis Platform for Efficient Preparation and Screening of Combinatorial Peptide Microarrays. Anal. Chem. 90, 5833–5840. https://doi.org/10.1021/acs.analchem.8b00371

Markarian, S.A., Terzyan, A.M., 2007. Surface tension and refractive index of dialkylsulfoxide + water mixtures at several temperatures. J. Chem. Eng. Data 52, 1704–1709. https://doi.org/10.1021/je7001013

Sutera, S.P., Skalak, R., 1993. The History of Poiseuille's Law. Annu. Rev. Fluid Mech. 25, 1–20. https://doi.org/10.1146/annurev.fl.25.010193.000245

Zong, D.M., Cinar, S., Shis, D.L., Josić, K., Ott, W., Bennett, M.R., 2018. Predicting Transcriptional Output of Synthetic Multi-input Promoters. ACS Synth. Biol. 7, 1834–1843. https://doi.org/10.1021/acssynbio.8b00165

Chapter 3 RoMI for protein network reconstitution

3.1 Abstract

Protein networks can be assembled *in vitro* for basic biochemistry research, drug screening, and the creation of artificial cells. However, the traditional well plate-based methods have fundamental limitations for the assembly of protein networks due to the lack of membrane confinement or attachment. Furthermore, the current microfluidics-based platforms have limited flexibility for varying the concentrations of multiple protein components. We have addressed the challenge by engineering a microfluidic printing robot. The new printing robot has automated multi-reagent processing capability and disposable microfluidic cartridge design, such that it can exchange multiple cartridges in sequence without cross-contamination. Importantly, the robot can print droplets (1 μL) at 1-2 orders of magnitude lower than that of the conventional well plate-based methods. The robot allows the assembly of protein networks in water-in-oil droplets with different concentration profiles. It also enables the study of protein networks in both membrane-unbound and -bound states. We demonstrate the robot using a sub-network of mitogen-activated protein kinase (MAPK) containing MEK or/and ERK kinase. The current system provides a labor-free, reagent-saving, efficient and flexible way for protein network research and related applications.

3.2 Materials and Methods

3.2.1 Microfluidic Printing Robot Integration

Microfluidic printing robot was built on a 4-DoF robotic arm (Magician, Dobot, Shenzhen, China). The robot arm was integrated with a pressure controller (PG-MFC, PreciGenome, San Jose, CA) and a custom-made valve controller. The valve controller was based on Arduino architecture with two mini solenoid valves (LHDA1221111H, Lee Co, Franklin, TN). The robotic arm was equipped with a two-finger gripper that applied a horizontal force using an embedded air pump in the robot. A pair of customized 3D-printed connectors were mounted on the robotic gripper that served as a seamless pneumatic connection between the robot and the microfluidic cartridge. As a result, the compressed air could be introduced from the robot to the cartridge controlled by the valve control circuit with the sub-millisecond resolution. The system was communicated and controlled by a computer via USB ports in a programmable manner (Python, Python software foundation, Beaverton, OR). More details of the fully automated liquid handling process have been described in the previous work(Wang et al., 2019).

3.2.2 Microfluidic Print-Head Fabrication

The microfluidic cartridge consisted of a 3D-printed reservoir/macrochannel layer, a double-adhesive microchannel layer, and a micronozzle layer. The cartridge could store 200 µL of reagent volume in the reservoir. The reservoir/macrochannel layer was designed in SolidWorks software and fabricated with a Clear Resin (Formlabs) using SLA 3D printer (Formlabs Form 3). The double-adhesive microchannel layer (ARcare® 90445, Adhesives Research, thickness of 80 µm) was designed in AutoCAD, and laser-cut (Universal Laser Systems, VersaLaser 2.30) to form the microchannel with a width of 200 µm. The micronozzle layer was fabricated by drilling 80 µm through-holes on a PMMA sheet (Nuowei, Shenzhen, thickness: 75 µm). These three layers were aligned and assembled layer by layer under an inverted stereoscope.

3.2.3 Microarray Substrate

Polydimethylsiloxane (PDMS)-coated cover glass (60×48 mm, Gold Seal®, cat. 48404-142, VWR, Radnor, PA) was used as the array substrate. PDMS was prepared using a 10:1 (w/w) mixture of the base to a curing agent (SYLGARDTM 184, Dow Corning), spin-coated on the cover glasses at 1000 r.p.m. for a 90 μm thick layer, and then cured on a hot plate at 120 °C for 1 hour. PDMS served as a hydrophobic substrate for the formation of water-in-oil droplets (water contact angle is >100°)(Mata et al., 2005).

3.2.4 Multiplexed Water-in-oil Droplet Microarray Formation

Before printing, the humidity was kept at 40%-50% using a humidifier. The printing parameters were set in an Excel file for each reagent, including starting position, row and column distances, row-column matrix, and the number of accumulated droplets. All fresh reagents were loaded into the reservoir of the microfluidic cartridges through the side inlet by manual pipetting right before printing. Once grabbing the target reagent from the designated position, a calibration step was set to dispense droplets. Thus, we could visualize the performance of the cartridge. After that, the robot executed the printing task instructed by the Excel file. In our test, both row and column distances were set as 3 mm. The total droplet volume in each site was <1 μL for maintaining the droplet shape. A1.5 mm-thickness acrylic sheet (Amazon, Vacaville, CA) and a double adhesive sheet were cut with a laser machine and assembled into the customized-size frame. After printing, we placed the customized frame around the entire printed droplets and added lipid-dissolved oil over the droplets gently. The estimated oil volume was about 25 μL per droplet. A schematic diagram of the entire process of forming multiplexed water-in-oil droplets is shown in Fig. 3-1.

3.2.5 Preparation of lipid-containing oil

Two different types of lipids were purchased from Avanti Polar Lipids (AL, USA), L-α-phosphatidylethanolamine (cat. 840021C, Egg PE), and 1,2-dioleoyl-sn-glycero-3-[(N-(5-amino-1-carboxypentyl) iminodiacetic acid) succinyl] (nickel salt) (cat. 790404C, DGS-NTA(Ni)), which were used without further purification. Paraffin oil was purchased from Fisher Scientific (cat.

AC444180250, Waltham, MA). Two different lipids in different concentrations were mixed in small glass vials, dried under a gentle stream of nitrogen, and then kept under a vacuum for roughly 3 hours. Completely dried lipids were resuspended in the paraffin oil, followed by shaking (200 r.p.m.) at 30 °C overnight. The final concentration of Egg PE was 0.5 mM, while 0-0.1 mM DGS-NTA(Ni) were selectively added for different tests. The dissolved lipids in paraffin oil remained stable at room temperature for around one week.

3.2.6 Droplet Characterization

The printed droplet volume was characterized by the methods of imaging and weighing analysis. The images of droplets were taken under a bright field microscope (EVOS XL, Life Technologies, USA). The diameters of the droplets (on a PDMS array substrate in Fig. 3-2a) were measured through the particle analysis function in ImageJ software (NIH, Bethesda, MD). We estimated the droplet volume by assuming that each droplet is a hemispherical shape with a contact angle of 109° on the substrate (Fig. 3-2b). We weighed it after dispensing 100-1000 times droplets (Fig. 3-2c-d) into a container with mineral oil under a 4-digital microbalance (Mettler Toledo AB54-S/FACT). In Fig. 3-2c, the printing pressure was consistent, but the total printing number changed. In Fig. 3-2d, the printing pressure was adjusted for printing 100 droplets. Through the weighing analysis, we enabled to characterize the droplet volume and the volume linearity. As shown in Fig. 3-2c-d, the total printed droplet weight converted to total printed volume according to the water density (0.996 g/mL) and 20% v/v glycerol in water density (1.051 g/mL) and further averaged into a single droplet volume as required.

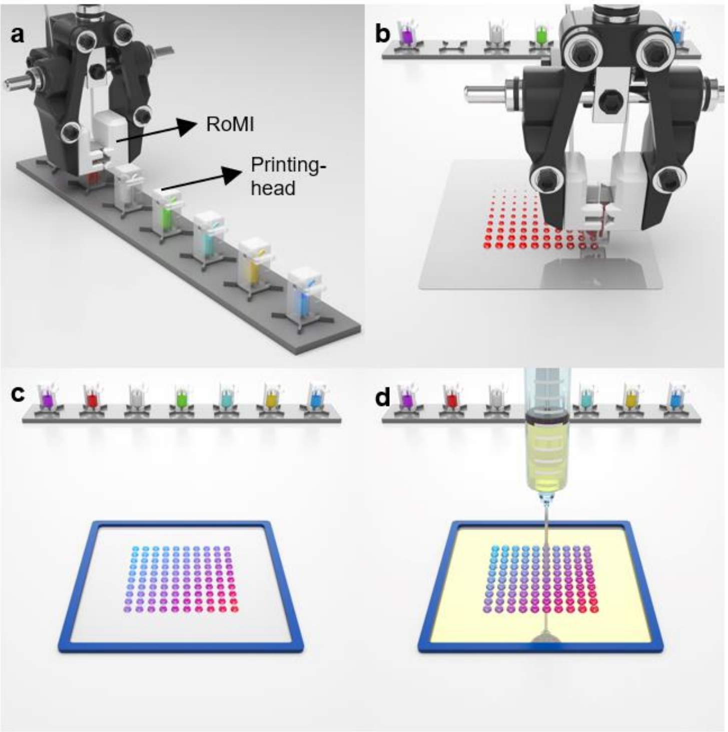

Fig. 3-1 Schematic of the entire process for forming multiplexed water-in-oil droplets. a) The microfluidic robot grips the target cartridge and forms a seamless robot-microfluidic interface (RoMI); b) The cartridge generates a droplet array under the control of RoMI; a–c) are repeated until the multiplexed droplet array is formed as shown in c) and an adhesive-customized frame is placed around the entire printed droplets; d) lipid-containing oil is added onto the lipids to form a phospholipid layer around the droplet.

3.2.7 Purified Protein reagents

For visualizing the protein distribution in the water-in-oil droplet, we purchased recombinant proteins, Aequorea Victoria Green Fluorescent Protein (GFP) His-tag (cat. A42613, Thermo Fisher Scientific, MA) and Cy5-streptavidin (PA45001, GE Healthcare). Both proteins were diluted with a PBS buffer (pH = 7.4) before testing. In the proof-of-concept experiment, the proteins (ERK2, MEK1_R4F, and phosphorylated ERK2) were expressed and purified from Dr. Jiyoung Shim.

3.2.8 MEK or/and ERK activity assay *in vitro*

We used the PhosphoWorksTM Fluorimetric ADP assay kit (cat. 21655, AAT Bioquest, CA) for assaying MEK-ERK network by monitoring red fluorescence intensity due to the ADP formation. We followed the manufacturer's protocol. Briefly, we added 10 µL of the protein solution to 5µL of ADP Sensor and 10 µL of ADP Sensor Buffer for using a fluorescence microplate reader (Tecan M1000Pro, Männedorf, Switzerland). The protein solution contained: 1 µM MEK_R4F and 2.5 µM ERK2 substrate were separately prepared in the kinase buffer (50 mM Tris/HCl (pH 7.4), 150 mM NaCl, 10 mM MgCl2, and 1 mM ATP)(Pirman et al., 2015). The mixture (Protein solution, ADP Sensor and Buffer) was added to each well of a black flat-bottom 384-well microplate (cat. 781096, Greiner Bio, NC) and monitored for the red fluorescence at 30 °C with shaking (orbital, 1 min every 5 min) for 2 hours. The excitation and emission wavelengths for the ADP sensor were 540 and 590 nm, respectively. After monitoring red fluorescence intensity, we examined ERK2 phosphorylation by MEK1 (R4F) mutant(*) in the same reaction using immunoblot analysis.

3.2.9 Western blotting-based assay

A 9 mL of the reaction was mixed with 2X Laemmli sample buffer (cat. 1610737 Bio-Rad, CA), and then heated to 55°C for 10 minutes after we finished monitoring the ADP assay using a microplate reader. All the samples were prepared in the same manner except for pERK2. The positive control, pERK2, was diluted to be 0.1 mM and made ready for running SDS-PAGE gel. All reactions were loaded and run on 12-well 4-20% pre-casted SDS-PAGE gel (cat. 4561095DC, Bio-Rad, CA). The proteins were transferred to a PVDF membrane (cat. 1620174, Bio-Rad, CA) and verified by blotting with 1:10,000 of p44/42 MAPK-mouse mAb (cat. 4696, CST, MA) and p47hospho-p44/42 MAPK-rabbit mAb (cat. 4370, CST, MA) respectively, followed by mouse-

HRP (cat. 31430, Thermo Fisher Scientific, MA) and rabbit-HRP (cat. 7074, CST, MA). The chemiluminescent signal was detected using a CCD camera after exposing the membrane to the Western ECL Substrate (cat. 1705061, Bio-Rad, CA) for 5 minutes. This assay was repeated four times from the individual sample sets.

3.2.10 MEK or/and ERK activity assay *in-vitro* Automated Assembly

For using the microfluidic printing robot, we prepared four cartridges: kinase buffer (50 mM Tris/HCl (pH 7.4), 150 mM NaCl, 10 mM MgCl2, and 1 mM ATP)(Pirman et al., 2015), 2.5 µM ERK2 WT substrate in the kinase buffer, 1 µM MEK1 (R4F) * in the kinase buffer, and the combination of ADP Sensor mix. We multiplexed the input reagent by printing additional droplets to the preformed one at ambient temperature. We allotted the same amount of the ADP Sensor mix but varied the concentration of the kinase proteins in each droplet. After printing four reagents with different volume ratios, the final volume of the droplet was almost 1µL. We used a fluorescence microscope to monitor the protein activity alone and the protein network reaction.

3.2.11 Fluorescence microscope Image Acquisition and Analysis

The water-in-oil droplets on the microarray were observed under an inverted microscope (Nikon Eclipse Ti-E). For the His6-tagged GFP and Cy5-streptavidin tests, a green filter cube (525 nm emission) was used to measure the GFP fluorescence and a purple filter cube (648 nm emission) was used to measure the Cy5 fluorescence. For the MEK-ERK network, a red filter cube (605 nm emission) was used to obtain the red fluorescence signals. All droplet locations were assigned, and then the droplet image was automatically taken individually at 30 °C for 1 hour every 10 min. All the microscope images were converted to a tiff image file using NIS-Elements Viewer 5.21 64-bit.

The fluorescence intensities were quantitated by calculating the average red value while filtering out the black background using the OpenCV library (Python version 3.7).

3.3 Results and Discussion

3.3.1 Printed droplet volume is consistent

To evaluate the consistency of the single droplet volume, we analyzed a single water droplet volume distribution (n=60, Fig. 3-2b) on a PDMS substrate (Fig. 3-2a). Specifically, 83.3% of the droplets are in the range of 52-61 nL, of which 58-61 nL droplets are the most, accounting for 40.0% of the droplets. The diameter CV (coefficient of variation) of the droplets is 2.1%, and the droplet volume CV is 6.2%. These results show the high uniformity of the single droplet, which is comparable to that of expensive piezoelectric-based droplet dispensers.(Fan et al., 2018) Therefore, the desired volume (in a discontinuous manner) can be determined by the droplet number.

To further ensure the printing stability of the microfluidic robot, we measured (Methods M6) the total weight of different droplet numbers, ranging from 100 to1000 in Fig. 3-2c. The total droplet volume was linearly proportional to the droplet number, with a correlation coefficient of 0.9999. In particular, the slope value was 0.0592, indicating the single droplet volume was around 59.2 nL. The results showed that the microfluidic printing robot could stably print thousands of droplets, and the average droplet volume from every 100 droplets is consistent.

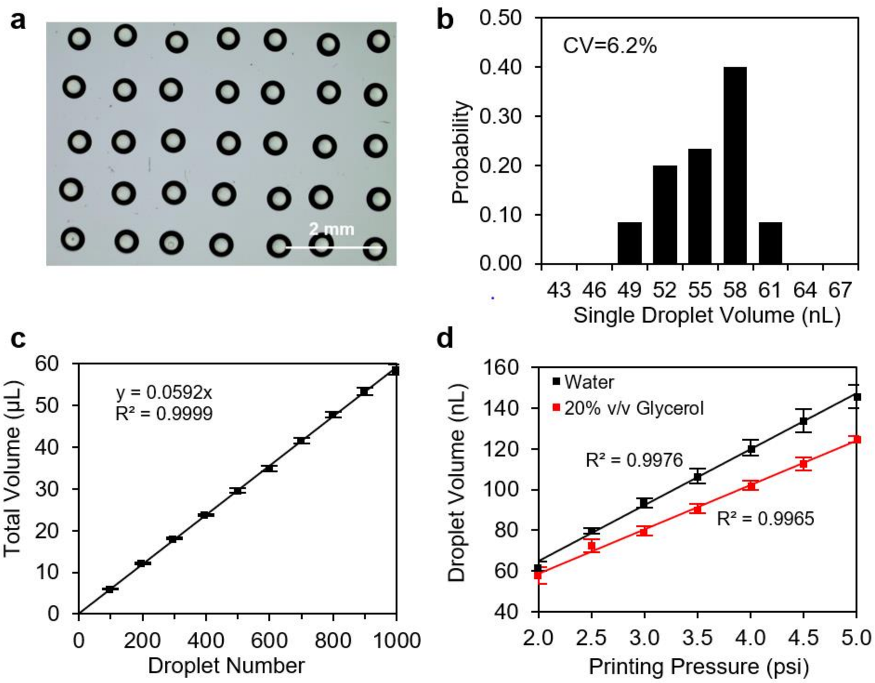

Fig. 3-2 Validation of printed droplets by the microfluidic printing robot. a) The microscopic image of a droplet array; b) the single droplet volume distribution (n=60); c) linearity of the total droplet volume of 100-1000 droplets, with a R2 > 0.9999; d) the averaged single droplet volume under various printing pressure from 2.0 to 5.0 psi. Black indicates water droplet. Red indicates 20% v/v glycerol droplet.

In addition, we tested the effect of printing pressure on droplet volume (Fig. 3-2d). The droplet volume was increased as printing pressure increased for both water and 20% v/v glycerol-in-water, with a high correlation coefficient R2 = 0.9976 and R2 = 0.9965, respectively. Specifically, the water droplet volume was 62.3 nL at 2 .0 psi and 145.6 nL at 5.0 psi, and the 20% v/v glycerol-in-water volume was 57.7 nL (7.38% decrease) at 2.0 psi and 124.8 nL (14.29% decrease) at 5.0 psi. Thus, the calibrated printing pressure for 20% v/v glycerol-in-oil was 2.2 psi for printing ~60 nL, while for water was 2.0 psi. Therefore, for most water-based reagents (e.g., PBS buffer, kinase buffer mentioned above), 2.0 psi printing pressure was used in all the following experiments.

We also aim to create droplets that mimic the spherical shape of natural cells. Hence, we analyzed the shape of the droplets (containing 0.25 µM His-tag GFP) in the oil w/ and w/o 0.05 mM DGS-

NTA(Ni). As shown in Fig. 3-3, the estimated contact angle is 137.6 ± 3.1 degrees, and the surface area of the water-oil interface accounts for 86.9% ± 1.9% of an ideal complete sphere. As a result, the water-in-oil droplet is close to a spherical shape. Since the contact surface might affect the signaling pathways underlying cellular adhesion, detachment, and communication, our microfluidic robot could generate reaction environments that are more suitable for protein network studies than standard well-plates.(Ferrari et al., 2019)

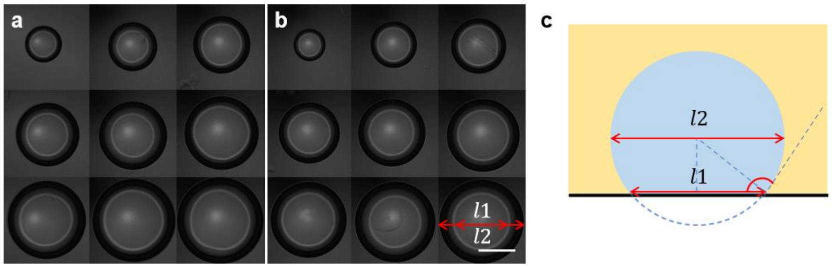

Fig. 3-3 Droplet shape analysis. Brightfield images of 1-9 droplets of 0.25 µM His-tag GFP in 0.5 mM Egg PE paraffin oil containing (a) 0 and (b) 0.05 mM DGS-NTA(Ni), scale bar: 500 µM. (c) The measured *l*1and *l*2 were used to estimate the contact angle and the surface area ratio of the water-in-oil interface (assuming the droplet is a part of a sphere shape).

3.3.2 Proteins can bind to the membrane of droplets

Next, we investigated if a functional membrane interface could be formed on each droplet. We printed five sets of droplet arrays containing 0.25 µM His6-tagged GFP with different droplet sizes and added paraffin oil containing 0.5 mM Egg PE and with the different concentrations of 0, 0.0125 (2.5%), 0.025 (5%), 0.05 (10%), 0.1 (20%) mM DGS-NTA(Ni) (Fig. 3-4a). As a negative control group, in the absence of DGS-NTA(Ni), green fluorescence was evenly distributed in each droplet. However, in the presence of the DGS-NTA(Ni), His6-tagged green fluorescence protein accumulated at the interface of the droplets. The green fluorescence signal became stronger at the interface and darker inside the droplet from left to right as the concentration of DGS-NTA(Ni) was increased from 0 to 0.1 mM. The results indicate that more DGS-NTA(Ni) in the oil is beneficial to immobilize His6-tagged protein at the interface. Therefore, we used 0.1 mM DGS-NTA(Ni) in the following experiments. However, no difference was observed by changing the droplet size, ranging from 0.24 µL to 0.96 µL, under the same concentration of DGS-NTA(Ni). Thus, these results show that the His6-tagged protein immobilized at the interface of the droplet after supplementation of DGS-NTA(Ni)-containing oil over the droplets.

Next, we investigated the saturation of binding sites on the membrane interface. We studied the distribution of different concentrations of His6-tagged GFP proteins under two different oils without and with DGS-NTA(Ni) (Fig. 3-4b). We printed two sets of 0.6 µL droplet arrays containing different concentrations of GFP, ranging from 0 to 1.0 µM, and added paraffin oil containing 0.5 mM Egg PE without and with 0.1 mM DGS-NTA(Ni). In the absence of the DGS-NTA(Ni), the green fluorescence was distributed uniformly in all droplets, and the green fluorescence signal became brighter as the protein concentration increased. In the presence of the DGS-NTA(Ni), His6-tagged GFP (0.25 µM) was bound at the interface. However, when the GFP concentration further increased, even with 0.1 mM DGS-NTA(Ni), the fluorescent signal inside the droplet became stronger. The result suggests that binding sites at the interface of the droplet are limited. When the binding sites are saturated, the excess protein is distributed inside the droplet. In conclusion, when the His-tag protein concentration is lower than 0.5 µM, most of the His6-tagged proteins in the droplets are immobilized at the interface with 0.1 mM DGS-NTA(Ni).

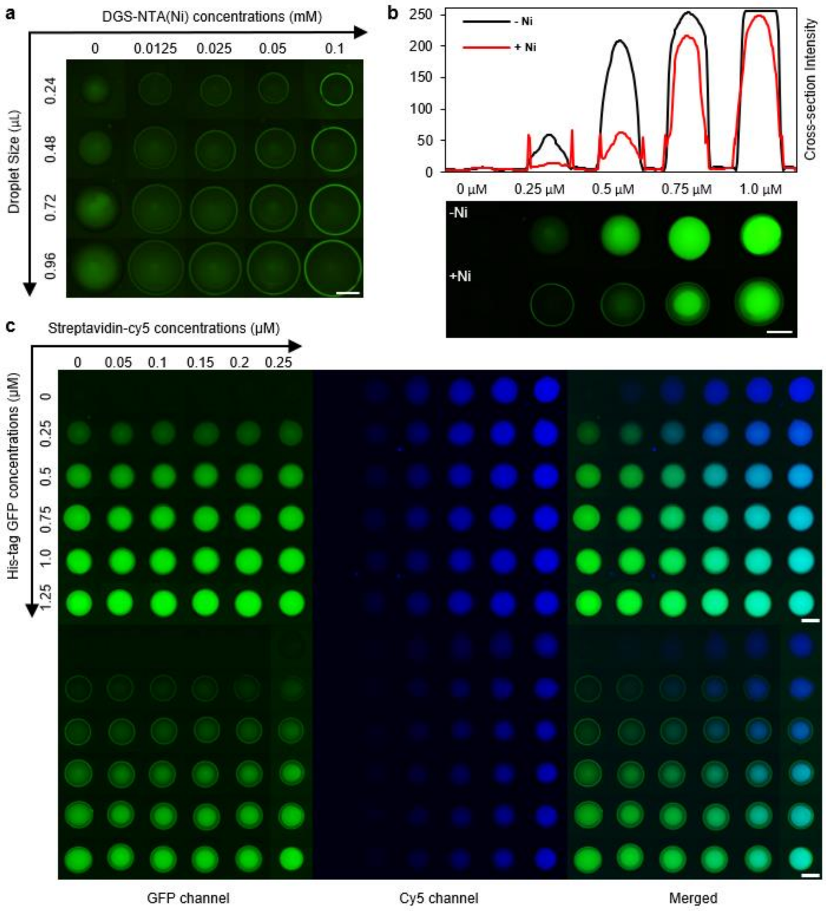

Fig. 3-4 Printed droplet arrays using fluorescent probes. a) Fluorescent images of 0.24, 0.48, 0.72 and 0.96 µL droplets containing 0.25 µM His-tag GFP under 0, 0.0125, 0.025, 0.05, 0.1 mM DGS-NTA(Ni); b) Fluorescent images and cross-section fluorescent intensities of 0.48 µL droplets containing 0, 0.25, 0.5, 0.75 and 1.0 µM His-tag GFP under 0 (black curve) and 0.1 mM (red curve) DGS-NTA(Ni); c) GFP channel, Cy5 channel and Merged (GFP and Cy5) results from the combinatorial droplet array with His6-tag GFP (0-1.25 µM), streptavidin-Cy5 (0-0.25 µM), and PBS buffer (pH=7.4) under 0 (Top, -Ni) and 0.1 mM (Bottom, +Ni) DGS-NTA(Ni). Scale bar: 500 µM. (GPF images: 1s exposure time, Cy5 images: 500 ms exposure time).

To ensure the precise control of protein localization inside each droplet, we measured the localization of His6-tagged GFP and streptavidin-Cy5. As shown in Fig. 3-4c, we printed two sets of 6 by 6 matrices and added oils without DGS-NTA(Ni) (-Ni) and with 0.1 mM DGS-NTA(Ni) (+Ni), respectively. From the first row to the sixth row, there were 0, 1, 2, 3, 4, and 5 droplet ejections of 2.5 µM His6-tagged GFP solution, and from the first column to the sixth column, there were 0, 1, 2, 3, 4 and 5 droplet ejections of 0.5 µM streptavidin-Cy5. By the additional droplet ejections of PBS buffer (pH=7.4) to the preformed droplets, each site contained 10 droplet ejections with a total volume of 0.6 µL. From all the images in Fig. 3-4c, both the fluorescence signals from the GFP channel and the Cy5 channel gradually increased with the increased concentrations of His6-tagged GFP and streptavidin-Cy5. The consistent changes of the fluorescence signals showed that our method could accurately control the two different protein concentrations in each droplet. In the case of +Ni, His6-tagged GFP was immobilized at the interface of the droplet, while Streptavidin-Cy5 was distributed evenly inside the droplet. The result verifies the specificity of the binding affinity between the His6-tagged proteins and DGS-NTA (Ni). Overall, our robotic platform can control the protein concentration profiles in the droplet and allow His6-tagged proteins to bind to the DGS-NTA(Ni) at the membrane interface.

3.3.3 Well-plate assays of MEK1 (R4F) or/and ERK2 proteins

Before testing the MEK-ERK activities in droplets, we validated their kinetics using traditional well-plate and western-blot assays. As shown in Fig 4a, ATP was converted to ADP in the presence of protein kinases, then converted back to ATP in the presence of the ADP assay kit(cat. 21655, AAT Bioquest, CA).(Lian et al., 2014) The ADP assay kit detects the produced amount of the ADP indirectly through the reaction of enzyme cascades. As a result, the rate of horseradish peroxidase (HRP) activity could be measured by a fluorescent probe(Lian et al., 2014). The ATPase activity (ATP hydrolysis) of the proteins was evaluated using a microplate reader (Method M9). A total amount of 25 µL solutions were used with 60% volume of the ADP sensor mix and 40 % volume of kinase containing samples to have the final concentrations of no kinase, 0.2 mM of MEK1 (R4F)*, 0.5 mM of ERK2 WT, and the combination of both (COM) (Fig. 3-5b). The brightest red fluorescence signal was observed in the combination group, followed by MEK1 (R4F) alone, ERK2 WT alone, and no kinase (buffer only – negative control). The red fluorescence intensity increased until it plateaued. The kinase buffer group (background trace) is significantly different from other samples. 0.5 µM ERK2 WT is significantly different from COM (0.5 µM ERK2 WT + 0.2 µM MEK1*). However, there is no significant difference between 0.5 µM ERK2 WT and 0.2 µM MEK1* and between 0.2 µM MEK1* and COM. We analyzed the data using a two-tailed t-test ($P < 0.05$, n=4) and a one-way ANOVA ($P = 0.00023$). The results proved the ATPase activity of the COM group, as well as ERK2 WT alone and MEK1 (R4F)* in the absence of the protein substrate. The ATPase activity of the single protein groups is consistent with literature data. A prior work estimated ATPase kinetic constants of phospho-MEK alone and phospho-MEK-ERK. The catalytic efficiency (kcat/KM) of phospho-MEK alone is ~ 3-fold higher than that of phospho-MEK-ERK(Rominger et al., 2007). Furthermore, the overall catalytic rate of phosphorylated ERK2 is higher than that of the unphosphorylated ERK2(Wang et al., 2002). The combination of these two effects may explain the fastest ATP hydrolysis rate of the COM sample, but the rate was not significantly different from the MEK1*. Altogether, consistent with literature data, COM exhibits the highest ATPase activity, followed by MEK1*, and then ERK2 WT, although the concentration of MEK1* is 2.5-fold lower than ERK2 WT.

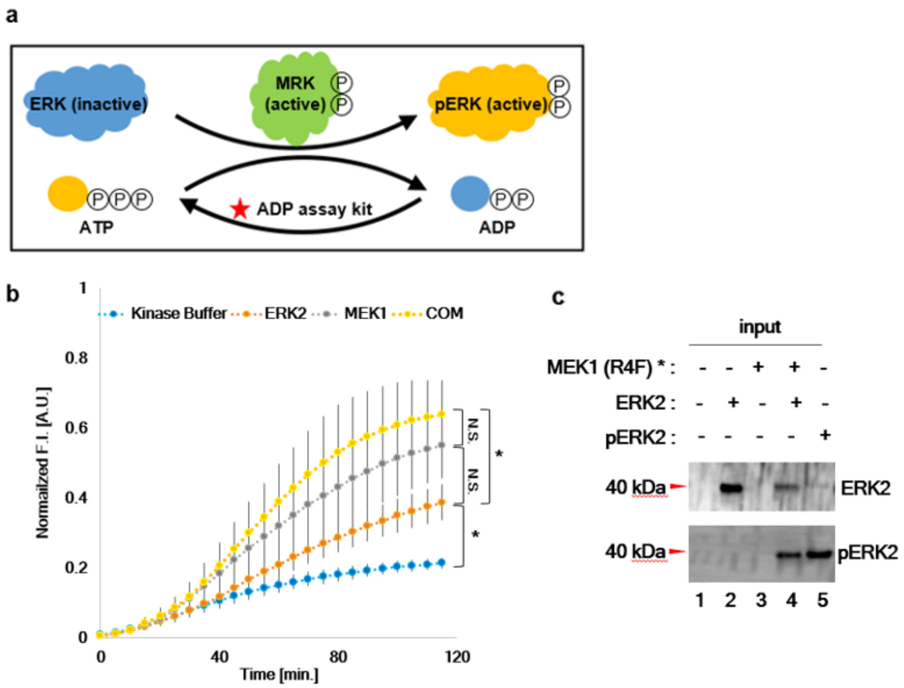

Fig. 3-5 Validation of MEK-ERK activities in well-plate assays. a) Schematic diagram of the MEK-ERK protein network activities; b) The ATPase activities were examined using a microplate reader. Error bars represent ±SD from the mean of four independent experiments (n = 4). Two tailed t-test (*, $P < 0.05$; significance difference between two groups, N.S.; no significant difference); c) Immunoblot analysis of proteins with antibodies against indicated kinase proteins. The cropped panels were taken from the same reaction after the fluorescence signal read-out in b.

We next sought to explore the kinase activity underlying this ATPase activity right after the fluorescence read-out using western blots (Method M10). In parallel, the purified pERK2 was added next to the COM for comparison. As shown in Fig 4c, ERK2 WT was detected in the ERK2, COM, and pERK2 groups. pERk2 was identified in the COM and pERK2 groups. Thus, both ERK2 WT and phosphorylated ERK2 were detected in the COM group and the pERK2 (positive control) group, while phosphorylated ERK2 was not found in the only ERK2 sample. The western blot data demonstrated the MEK1 (R4F)-mediated phosphorylation of ERK2 in the COM group.

3.3.4 Kinase screening in droplets using the printing robot

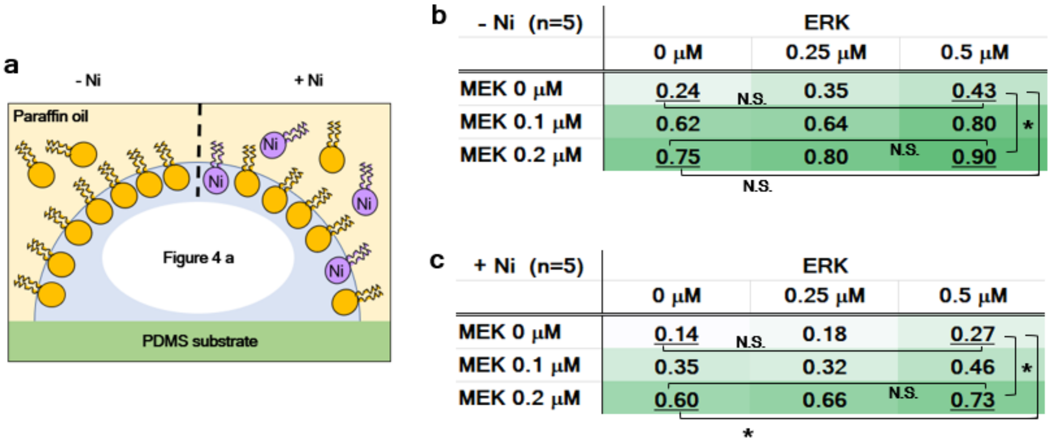

b

- Ni (n=5)	ERK 0 μM	ERK 0.25 μM	ERK 0.5 μM
MEK 0 μM	0.24	0.35	0.43
MEK 0.1 μM	0.62	0.64	0.80
MEK 0.2 μM	0.75	0.80	0.90

c

+ Ni (n=5)	ERK 0 μM	ERK 0.25 μM	ERK 0.5 μM
MEK 0 μM	0.14	0.18	0.27
MEK 0.1 μM	0.35	0.32	0.46
MEK 0.2 μM	0.60	0.66	0.73

Fig. 3-6 Validation of MEK-ERK activities in droplets with and without membranes. a) Schematic illustration of the water in oil droplet included a) reactions without (-Ni) and with 20% DGS-NTA (Ni) (+Ni). b & c) ADP screening results. Normalized F.I. from two-dimensional dilution of both ERK2 WT and MEK1 * b) without (-Ni) and c) with 20% DGS-NTA (Ni) (+Ni).

We next sought to examine the ATPase activity of full-length MEK1 (R4F)* and ERK2 WT using our combinatorial droplet printer. We utilized four print heads to mix four reagents (kinase buffer, 1 mM of MEK1 (R4F) *, 2.5 mM of ERK2 WT, and ADP sensor mix) in different ratios. In each droplet, 0.6 mL out of 1 mL was allotted to the ADP sensor mix, which left 0.4 mL for multiple dilutions of protein kinase. To dilute the kinase, we printed the solutions sequentially using different amounts of kinase and kinase buffer solutions. We designed a 3 by 3 combinatorial array. Furthermore, we supplemented oil with and without 20% DGS-NTA (Ni). Oil with 20% DGS-NTA allowed selective membrane attachment of the kinases (Fig. 3-6a). All the data were normalized within each screening assay because the ADP sensor is temperature and time sensitive. We compared the means from each concentration group to analyze the data (n=5) with a one-way ANOVA for both unbound ($P < 0.000005$, -Ni) and bound ($P < 0.00002$, +Ni) kinase categories.

We made two unique observations about the kinase assay in microliter droplets. First, the kinase concentration was not saturated in our assay because a higher concentration of both protein kinases (ERK2 WT or/and MEK1 *) produced a higher fluorescence intensity (Fig. 3-5b, 3-6b, and 3-6c). Second, our statistical analysis results confirmed the slightly higher ATPase activity in the -Ni category compared to +Ni at the same condition for all concentration groups. The results likely arise due to the diffusion limited reaction of the kinases in the localized state at the interface versus in a free state.

Otherwise, the droplet assays show consistent results with the well-plate assays. In each category, the kinase buffer (no kinase at all) showed a statistical difference from other groups that contain at least 0.1 μM MEK1 * in the -Ni category (Fig. 3-6b, $P < 0.05$). The kinase buffer also showed a statistical difference from the COM (0.1 μM MEK1* + 0.5 μM ERK2) as well as the groups that contain at least 0.2 μM MEK1 in the +Ni category (Fig. 3-6c, $P < 0.05$). These differences from the negative control proved the ATPase activity of ERK2 WT and MEK1 (R4F) *. The highest ATPase activity was shown in the COM (0.5 μM ERK2 + MEK1 *) without the significant difference from the only MEK1 * except 0.1 μM MEK1* in the -Ni category ($P < 0.05$). Through these results of combinatorial droplet microarray, we have demonstrated the kinase (ATPase) activity of MEK1 (R4F) * and ERK2 WT individually and together, with the selective membrane attachment of the kinases.

3.4 Conclusions

In summary, we have introduced the microfluidic printing robot for the high-throughput assembly and screening of a kinase pathway *in vitro*. The microfluidic printing platform enables multiparametric studies through a few unique features (i) automated printing of microarray (ii) generation of the concentration gradient (iii) combinatorial multiplexing (iv) the microfluidic cartridges are inexpensive and disposable (cross-contamination free), (v) high printing speed/throughput in precise-controlled nanoliter droplets, (vi) it forms biomimicry spherical and membrane environment. Moreover, we endow the option of selective membrane attachment by using his6-tagged purified proteins. Quantitative results show that more His6-tagged GFP was immobilized at the interface as the higher concentration of DGS-NTA(Ni) was used. In addition, the His6-tagged GFP was immobilized at the interface, while none-His6-tagged streptavidin-Cy5 was distributed evenly inside the droplet. Our result verified the protein rearrangement according to the binding affinity specifically. Furthermore, both green and Cy-5 fluorescence signals became stronger proportionally to the dose amount of the fluorescent molecules.

Applying the kinases to the microfluidic printing platform, we demonstrated the kinase activity of MEK1 * and ERK2 WT individually and together in the multi-combinatorial droplet microarray. ATPase activity was slightly higher in the membrane unbound kinase groups. The results from the well-plate and droplet assays were in fair agreement. The immunoblot analysis confirmed the phosphorylation of ERK2 by MEK1 *. The ATPase activity of a MEK1* is dominant compared to that of ERK2 WT despite much (2.5 times) lower concentration used. Overall, ATPase activity is enhanced proportionally as both kinase concentrations increase. The difference between the ATPase assay and immunoblot assay is consistent with literature data. As known, ATP hydrolysis by phospho-MEK1(Rominger et al., 2007) and some protein kinases (i.e., ERK2) perform ATPase activity by transferring the phosphoryl group (PO32-) to water(Roskoski, 2012). Our combinatorial microfluidic printing platform could be scaled up for screening protein kinase inhibitors with multi-kinases forming the signaling pathway in artificial cells. Furthermore, it may enable the systematic and high-throughput study of biochemical pathways for drug discovery.

References

Fan, J., Men, Y., Hao Tseng, K., Ding, Yi, Ding, Yunfeng, Villarreal, F., Tan, C., Li, B., Pan, T., 2018. Dotette: Programmable, high-precision, plug-and-play droplet pipetting. Biomicrofluidics 12. https://doi.org/10.1063/1.5030629

Ferrari, M., Cirisano, F., Carmen Morán, M., 2019. Mammalian cell behavior on hydrophobic substrates: Influence of surface properties. Colloids and Interfaces. https://doi.org/10.3390/colloids3020048

Lian, Q., Cao, H., Wang, F., 2014. The Cost-Efficiency Realization in the *Escherichia coli*-Based Cell-Free Protein Synthesis Systems. Appl. Biochem. Biotechnol. 174, 2351–2367. https://doi.org/10.1007/s12010-014-1143-4

Mata, A., Fleischman, A.J., Roy, S., 2005. Characterization of Polydimethylsiloxane (PDMS) Properties for Biomedical Micro/Nanosystems. Biomed. Microdevices 7. https://doi.org/10.1007/s10544-005-6070-2

Pirman, N.L., Barber, K.W., Aerni, H.R., Ma, N.J., Haimovich, A.D., Rogulina, S., Isaacs, F.J., Rinehart, J., 2015. A flexible codon in genomically recoded *Escherichia coli* permits programmable protein phosphorylation. Nat. Commun. 6. https://doi.org/10.1038/ncomms9130

Rominger, C.M., Schaber, M.D., Yang, J., Gontarek, R.R., Weaver, K.L., Broderick, T., Carter, L., Copeland, R.A., May, E.W., 2007. An intrinsic ATPase activity of phospho-MEK-1 uncoupled from downstream ERK phosphorylation. Arch. Biochem. Biophys. 464, 130–137. https://doi.org/10.1016/j.abb.2007.04.004

Roskoski, R., 2012. ERK1/2 MAP kinases: Structure, function, and regulation. Pharmacol. Res. https://doi.org/10.1016/j.phrs.2012.04.005

Wang, J., Deng, K., Zhou, C., Fang, Z., Meyer, C., Deshpande, K.U.A., Li, Z., Mi, X., Luo, Q., Hammock, B.D., Tan, C., Chen, Y., Pan, T., 2019. Microfluidic cap-To-dispense (μCD): A universal microfluidic-robotic interface for automated pipette-free high-precision liquid handling. Lab Chip 19, 3405–3415. https://doi.org/10.1039/c9lc00622b

Wang, Z.X., Zhou, B., Wang, Q.M., Zhang, Z.Y., 2002. A kinetic approach for the study of protein phosphatase-catalyzed regulation of protein kinase activity. Biochemistry 41, 7849–7857. https://doi.org/10.1021/bi025776m

Chapter 4 RoMI for sample-to-answer Robotic ELISA

4.1 Abstract

Enzyme-linked immunosorbent assays (ELISA), as one of the most used immunoassays, have been conducted ubiquitously in hospitals, research laboratories, etc. However, the conventional ELISA procedure is usually laborious, occupies bulky instruments, consumes lengthy operation time, and relies considerably on the skills of technicians, and such limitations call for innovations to develop a fully automated ELISA platform. In this chapter, we have presented a system incorporating a robotic-microfluidic interface (RoMI) and a modular hybrid microfluidic chip that embeds a highly sensitive nanofibrous membrane, referred to as Robotic ELISA, to achieve human-free sample-to-answer ELISA tests in a fully programmable and automated manner. It carries out multiple bioanalytical procedures to replace the manual steps involved in classic ELISA operations, including the pneumatically driven high-precision pipetting, efficient mixing and enrichment enabled by back-and-forth flows, washing, as well as integrated machine vision for colorimetric readout. The Robotic ELISA platform has achieved a low limit of detection (LOD) of 0.1 ng/mL in the detection of a low sample volume (15 μL) of chloramphenicol (CAP) within 20 min without human intervention, which is significantly faster than that of the conventional ELISA procedure. Benefiting from its modular design and automated operations, the Robotic ELISA platform has great potential to be deployed for a broad range of detections in various resource-limited settings or high-risk environments, where human involvement needs to be minimized, while the testing timeliness, consistency and sensitivity are all desired.

4.2 Working Principle

The Robotic ELISA system is designed to fully automate the entire ELISA workflow via the novel robotic-microfluidic interface (RoMI), which precisely positions the microfluidic chip, reversibly connects the pneumatic drives mounted on the robotic arm to the chip for automated liquid handling, and consecutively enables optical readout, followed by the waste disposal. Specifically, its operations include robotic loading, pipetting, mixing, washing, reaction, incubation, and colorimetric detection. As shown in Fig. 4-1a, the Robotic ELISA platform comprises three major components, namely the hybrid microfluidic ELISA chip, the robotic arm equipped with a pair of the RoMI effectors that incorporate pneumatic connectors for microfluidic control, and a high-definition vision unit for colorimetric detection.

First, the ELISA chip design has four major segments, that is, a serpentine channel connected to the chip tip for flow regulation, a detection chamber (with the nanofibrous membrane embedded inside), a planar buffer chamber, and a RoMI interconnect, as shown in Fig. 4-1b. The serpentine channel is connected to the detection chamber, which has an embedded nanofibrous membrane for the solid-liquid reactions, and the detection chamber is connected to the funnel-shaped liquid reservoir. The funnel shape is designed to aid the wetting of the side walls of the buffer chamber and avoid the trapping of air bubbles during the process of filling up. (de Gennes et al., 2004) In the microfluidic model to describe the fluid dynamics, the serpentine channel is designed to have significantly greater flow resistance than the rest. Therefore, during the aspiration of the reagents, the aspiration rate can be precisely controlled, according to the hydraulic Ohm’s law under laminar flow conditions, $\Delta P = R_f \cdot Q$, where ΔP is the pressure difference applied, Q is the flow rate, and R_f is the flow resistance, a geometrically governed and liquid-specific constant. (Oh et al., 2012)

Accordingly, the aspirated volume can be controlled, by precisely timing the duration of the aspiration using a high-precision solenoid valve that links to the RoMI effectors.

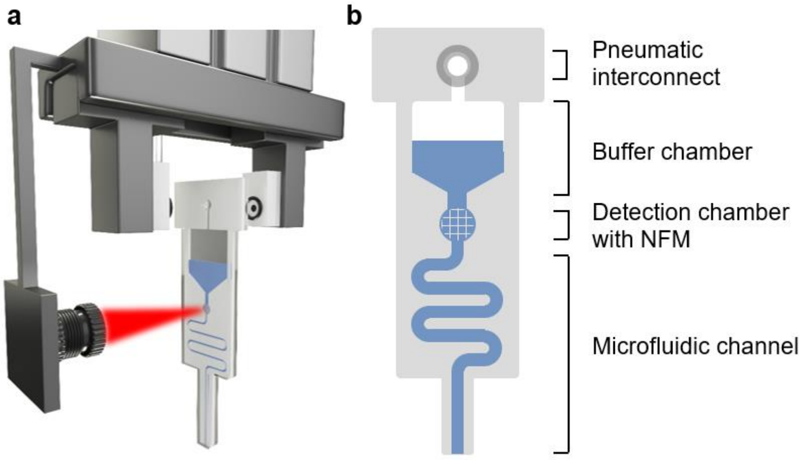

Fig. 4-1 Concept of the Robotic ELISA system. a) Illustration of the Robotic ELISA platform; b) illustration of the nanofibrous membrane (NFM)-contained hybrid microfluidic chip.

Second, on the robotic arm, the pair of the RoMI effectors are made from custom-designed and 3D-printed adapters to the robotic arm. (Wang et al., 2019) In particular, one side of the RoMI effector is connected to the pneumatic drive with precisely controlled pressure (either negative or positive) via a solenoid valve, while the other side can reversibly engage to the RoMI interconnect on the ELISA chip, upon gripping and clamping. As a result, the negative or positive pressure from the pneumatic drive can be directly applied to the microfluidic chip upon the gripping of the RoMI effector onto the chip, to perform the control of liquid handling. Third, the vision unit attached to the robotic arm can be used for the real-time colorimetric readout of the nanofibrous membrane inside the detection chamber. The imaging data can then be wirelessly transmitted and analyzed instantaneously.

As a demonstration, Fig. 4-2 depicts the use of the Robotic ELISA system in a standard competitive ELISA protocol, which includes the operations of high-precision metering, mixing, washing, enzymatic reaction, and robotic-vision enabled imaging and detection. First, the high-precision metering can be achieved through the pneumatically driven aspiration. (Oh et al., 2012) As aforementioned, the aspiration rate can be fine controlled by designing the serpentine channel with high flow resistance, and the aspiration volume can be adjusted by precise timing of the solenoid valve. Specifically, the process starts with sequential and quantitative aspiration of a sample solution (Fig. 4-2a) and a target conjugated horseradish peroxidase (target-HRP) solution (Fig. 4-2b), consecutively. Next, a mixing process can be achieved by alternately applying negative and positive pressure to the buffer chamber, thus aspirating the liquid through the device, similar to that of conventional pipette operations (Fig. 4-2c). In addition, the solutions can also sufficiently

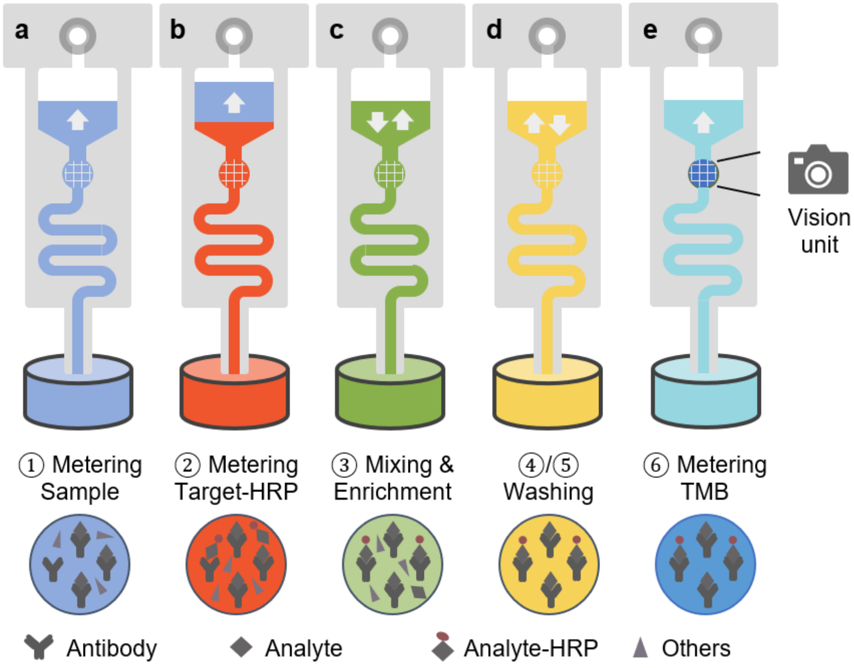

Fig. 4-2 Illustration of the Robotic ELISA operations, including a-b) high-precision metering, c) mixing and enrichment, d) washing, e) enzymatic reaction, and robotic vision unit enabled imaging and detection.

mix with the antibody-immobilized nanofibrous membrane inside the detection chamber during the aspiration, as the convective flow increases the chance of contact between the multiple samples and reagents with the membrane. As a result, the number of analytes bound to the antibodies can be increased and the incubation time is shortened. (Sanjay et al., 2020) As shown in Fig. 4-2d, efficient washing can be realized by a similar convective flow of the buffer solution enabled by the alternating pneumatic pressures. Finally, an enzymatic reaction is introduced by robotic loading of the colorimetric reagent of 3,3',5,5'-Tetramethylbenzidine (TMB) into the detection chamber in Fig. 4-2e. Following that, the vision unit on the robot is used to automatically record the real-time colorimetric change of the membrane, from which a recognition algorithm is applied to quantify the colorimetric results.

4.3 Materials and Methods

4.3.1 Integration of the Robotic ELISA system

The Robotic ELISA system mainly consists of three control modules: a professional SCARA robot arm (M1, Dobot), a pressure control unit (PG-MFC, PreciGenome), and a valve control unit that contains a valve manifold and high precision solenoid valves (LHDA2421111H, The Lee Company, USA). The system was communicated and con-trolled by a computer via USB ports in a programmable manner (with Python). Specifically, the robotic arm was programmed to grab, move, and release the hybrid microfluidic chip, with a maximum working range of 400 mm and a rated precision of 0.02 mm; the pressure control unit was programmed to set the pneumatic pressure level in the valve manifold within the range of -7 to 13 psi at a precision of 0.1 psi; the valve control unit was programmed to adjust the opening and closure duration of the solenoid valve with millisecond precision.

A pair of custom 3D printed RoMI effectors were de-signed to connect the air flow from the valve manifold to the RoMI interconnect on the hybrid microfluidic chip, with incorporated silicone rubber O-rings to ensure tight sealing. They were designed in SolidWorks and fabricated with a Clear Resin (Formlabs) using SLA 3D printer (Formlabs Form 3, USA). The RoMI effector linked the outlet of the valve manifold and the RoMI interconnect on the microfluidic chip. A test bench was set at the center of the robot arm's working area. A custom microplate adapter was fastened on the test bench and pre-calibrated. The images were captured in a programmable manner using a USB link between the lab PC and a miniature camera (HM1355, Banggood, USA). Prior to the measurements, by comparing with the membrane color in a reference device, the light source near the platform can be adjusted accordingly in order to achieve consistent brightness readouts of the sensing membrane. OpenCV library (Python version 3.7) was used to identify the periphery of the nanofibrous membrane inside the hybrid microfluidic chip and calculate the averaged grayscale value (color intensity) within the membrane. (Liu et al., 2015; Luo et al., 2019) In addition, the uniformity of the colorimetric readouts on the membrane were evaluated, by calculating the deviation of grayscale values.

4.3.2 Fabrication of the hybrid microfluidic ELISA chip

The nanofibrous membrane-contained hybrid microfluidic device can be prepared via laser micromachining and repetitive layer-by-layer (LBL) assembly. As illustrated in Fig. 4-3, the device consists of five layers, including three structural layers made of PMMA sheets (11510305 for 0.5 mm thickness and 11510310 for 1.0 mm thickness, Astra Products) and two layers made of pressure-sensitive adhesive (ARcare® 92712, Adhesives Research, Inc.), and the nano-fibrous membrane can be incorporated in the third layer. Specifically, the first layer is 1 mm thick and has a 1 mm opening that serves as the RoMI interconnect; the second layer has a thickness of 48 μm, with a serpentine microfluidic channel incorporated; the third layer has a thickness of 0.5 mm with a detection chamber (2 mm in diameter) for the nanofibrous membrane to reside and a buffer chamber to store the reagents; the fourth layer has a thickness of 48 μm and the fifth layer has a thickness of 1 mm. All the five layers were designed in AutoCAD (Autodesk Inc.) and laser-cut (Universal Laser Systems, VersaLaser 2.30) into the de-signed pattern. Each of the laser-cut layers was inspected under a microscope (EVOS XL, Life Technologies) and the channel width was measured and analyzed using ImageJ (National Institutes of Health). (Schindelin et al., 2012) Finally, the five layers were carefully aligned and assembled layer by layer under an inverted stereoscope.

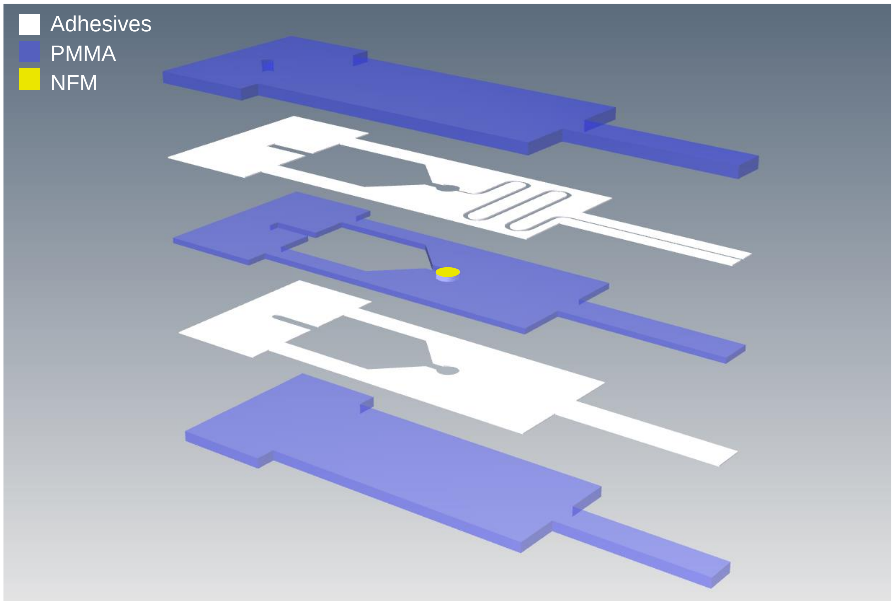

Fig. 4-3 Layer-by-layer (LBL) assembly of the microfluidic ELISA chip.

Table 4-1 Flow resistance of the key segments in the microfluidic ELISA chip

	d (mm)	w (mm)	L (mm)	h (mm)	Volume (µL)	Rf (Pa*s/mm^3)
Serpentine Channel	N/A	0.325	61.1	0.0467	0.93	2.17E+04
Detection Chamber	2.05	(≈1.07)	(≈2.05)	0.5850	1.93	1.02E-01
Buffer Chamber	N/A	4.53/7.98	3.49/8.56	0.5850	49.21	9.83E-02
Total					52.07	2.17E+04

4.3.3 Characterization of the hybrid microfluidic ELISA chip

To test the aspiration performance of the hybrid microfluidic device, DI water was used as the working fluid and a gravimetric method was used to determine the aspiration volume and aspiration rate. In particular, the tip of the ELISA chip was immersed underneath a microplate well filled up with water and a vacuum pressure (aspiration pressure from 0.5 to 3.0 psi) was applied to the RoMI interconnect of the device; the aspiration duration was precisely controlled with a solenoid valve, and the weight of the device before and after the aspiration process was measured with a high-precision balance (Mettler Toledo AB54-S/FACT). In such a way, the volume aspirated was determined, and the averaged aspiration rate was calculated by dividing the aspiration volume to the aspiration duration. It is worth noting that due to the hydrophilicity of the chip and capillarity of the liquid, a small amount of liquid (measured as 1.1 µL) was remained at the tip of the chip; such remained volume of liquid was deducted in the calculation to increase the accuracy of characterization.

In the optimization of washing cycles, enzymatic reaction, and enrichment flow and cycles, we adopted the same concentration and volume ratios of the samples and reagents as those utilized in our previous study. (Zhao et al., 2020) In the study of washing cycles, both membranes with or without the immobilized antibodies were prepared for different washing cycles, the enrichment flow was set at 2 psi and the enrichment cycle was 6. In the test of enzymatic reaction duration, the enrichment flow was set at 2 psi, the enrichment cycle was 6, and the washing cycle was 2. In the test of the enrichment cycle, the pressure for enrichment flow was 2 psi, the washing cycle was 2, and the enzymatic reaction duration was 6 min. In the test of the pressure for enrichment flow, the enrichment cycle was kept at 2 for all the various pressures under test, the washing cycle was 2, and the enzymatic reaction duration was 6 min. With an enrichment volume of 25 μL and the enrichment pressure of 1 psi, the net enrichment duration was 61.6 s for one cycle; at the pressure of 2 psi, the enrichment duration was 35.2 s for one cycle; at the pressure of 3 psi, the enrichment duration was 24.4 s for one cycle.

4.3.4 Demonstration of the automated sample-to-answer ELISA workflow

A competitive ELISA assay was designed and conducted for the automated detection of chloramphenicol (CAP) as a demonstration of the developed Robotic ELISA system. Chloramphenicol (CAP), florfenicol (FF), thiamphenicol (TAP), and penicillin (PCN) were obtained from Sigma Aldrich (USA). Different concentrations of CAP were prepared in PBS buffer (pH=7.4). The biological sample was obtained from salmon matrix using a recommended protocol for antibiotic extraction from food products. (Desmarchelier et al., 2018) Salmon samples (King salmon, Savory Alaska, Leander, TX) were homogenized in dry ice using Sears solid state 10-speed blender at speed 7. Briefly, 1 g of salmon homogenate was mechanically shaken with 8 mL water, 5 ceramic beads, 30 mL acetonitrile (A998-4, Fisher chemical) and 30 µl concentrated formic acid (F0507-1L, Sigma Aldrich) for 30 min at 200 rpm (Excella E24 incubator shaker series, New Brunswick Scientific). Then, pre-weighted salt mixture containing 4g Na2SO4 (798592, Sigma Aldrich), 1g NaCl (S7653, Sigma Aldrich) and 1.5 g of trisodium citrate dihydrate (A12274, Alfa Aesar) was added. The sample mix was shaken for another 30 min at 200 rpm. After centrifuging at 3000 rpm for 10 mins at 10 ˚C (SORVALL RT 6000D, rotor H1000B), 30 mL supernatant was dried under nitrogen and reconstitute in 1mL of water: methanol (1:1). The sample was further sonicated (Branson 1210, Danbury, CT) for 3 min, centrifuged (Eppendorf, 5424 R) at 12000 rpm (13523 ×g) for 2 min at 0 ˚C and filtered through Ultrafree-MC-VV PVDF filters (0.1 µm; Millipore Sigma). The sample was diluted ten times with PBS buffer (pH 7.4). Afterwards, 10 µL of CAP standard solution (containing 0, 2.5, 5 and 10 ng/mL CAP, respectively) was spiked into 90 µL of the diluted salmon sample extract, making the final concentrations of 0, 0.25, 0.5, and 1 ng/mL CAP, respectively.

The relevant testing reagents were preloaded in a standard 96-well microplate (GBO-655901, Greiner Bio-One Inc.), and then the microplate was sealed and stored at 4°C in the dark. In detail, as shown in Figure 2, such reagents include 30 µL of 0.5 µg/mL (1.0 µg/mL for optimizing washing cycles) HRP-CAP (50003, AAT Bioquest, USA) (Well ②), two 100 µL PBS washing buffer solutions (Well ④ & ⑤) and 30 µL TMB solution (ab171523, Abcam, USA) (Well ⑥). Before the assay, the reagent-loaded microplate was transferred to the fixed location of the microplate holder on the testing stage and then unsealed, following which a sample solution (30 µL or more) was added to the microplate (Well ①). Since the z-position deviation caused by the robot movement or chip manufacturing was about 200 µm, an extra volume of solution about 10 µL was added to the wells to ensure the effective contact of the tip of the ELISA chip with the liquid in the microplate wells. Such additional volume could be reduced by replacing the current microplates with wells that have smaller sizes.

In total, the sample solution and the relevant reagents occupied 6 wells. As shown in Figure 2, the entire competitive ELISA protocol includes six steps: 1) aspirating 15 µL sample solution from Well ①; 2) aspirating 15 µL HRP-CAP solution from Well ②; 3) mixing the sample and the HRP-CAP solution in Well ③ to induce a competitive reaction with the immobilized antibodies on the membrane, by pneumatically driving the mixture solution to flow through the membrane back-and-forth, and then withdrawing the mixture to the same well after the reaction; 4) aspirating and withdrawing washing solution (36 µL PBS buffer) to the membrane to wash and remove unbound proteins, in Well ④ & ⑤ sequentially, and then air-drying the membrane under a high air pressure of 4 psi for 30 s; 5) aspirating 10 µL TMB solution from Well ⑥ to induce the enzymatic reaction; 6) recognizing the membrane and recording the grayscale values for 10 min every 2 min. The sample size was three for all experiments.

4.4 Results and Discussion

4.4.1 Characterization of the aspiration process

As shown in Fig. 4-4a, the aspiration rates were determined under various pressure levels in the microfluidic devices with and without an incorporated nanofibrous membrane. For the devices without a nanofibrous membrane, the aspiration rate raised nearly linearly to the increment of the applied pressure, with a high correlation coefficient R2 = 0.999. Specifically, the aspiration rate was 0.19 µL/s at 0.5 psi, and it increased to 1.01 µL/s when the pressure level was elevated to 3.0 psi. These results were consistent with the prediction from the hydraulic Ohm's law. (Oh et al., 2012) Accordingly, the averaged flow resistance of the device could be computed, which was 20285 Pa·s/µL. On the other hand, the theoretical flow resistance could be calculated according to the analytical Poiseuille's equation under the laminar flow condition, for comparison. (Sutera and

Skalak, 1993) As described in detail in Table 4-1, the overall flow resistance was calculated approximately at 21677 Pa·s/μL, by considering resistances from the connecting serpentine microchannels, the detection chamber, and the liquid buffer chamber, of which the latter two were negligible. Though the theoretically determined flow resistance slightly deviated from (6.9%) the experimentally determined counterpart, it could offer a highly accurate approximation, which might be mainly altered by the dimensional (width and height) inaccuracies resulting from the microfabrication process. These results enabled that the aspiration rate could be conveniently adjusted by controlling the pressure applied.

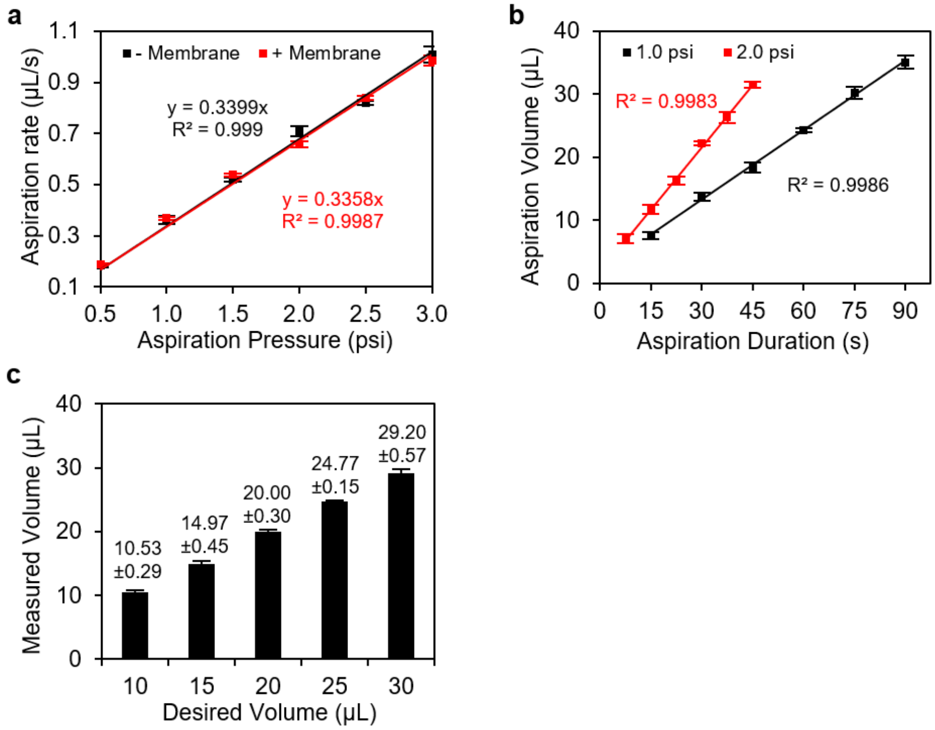

Fig. 4-4 a) The aspiration rates of the hybrid microfluidic chip under various pressure levels from 0.5 to 3.0 psi, with or without the nanofibrous membrane; b) the aspiration volume under various pulse durations from 10 to 90 s, given the pressure applied at 1 and 2 psi, respectively; and c) the measured accuracy of the aspiration volume for a desired volume from 10 to 30 μL.

Furthermore, we studied the control of aspiration volume by adjusting the pulse duration, as shown in Fig. 4-4b. At a fixed pressure of 1 psi, the aspirated volume was measured linearly proportional to the pulse duration, with a correlation coefficient of 0.9986. In particular, the aspiration volume was 7.6 μL at an applied duration of 15 s, and it was increased to 35.0 μL when the duration was extended to 90 s. Similarly, at a higher aspiration pressure of 2 psi, the aspirated volume was still found proportional to the aspiration duration with a correlation coefficient of 0.9983. The measured volume was 7.1 μL for 7.5 s of aspiration, and it was increased to 31.4 μL when the aspiration was extended to 45 s. In addition, at the same duration of 45 s, the aspiration volume was 18.4 μL for the aspiration pressure of 1 psi, while it was 31.4 μL for the pressure of 2 psi, approximately twice that of the 1 psi condition, as expected. These results confirmed that the aspiration rate was approximately constant at the fixed pressure, and the aspiration volume can be conveniently adjusted by varying the duration of aspiration. We further determined the accuracy of the duration-adjusted aspiration volume, as shown in Fig. 4-4c. First, the required duration of aspiration for a specific desired volume was deducted from the fitting curve in Figure 3b, which was 12.2 s for 10 μL, 19.9 s for 15 μL, 27.5 s for 20 μL, 35.2 s for 25 μL, and 42.9 s for 30 μL, respectively. Next, the actual aspirated volumes were measured, and they were 10.53 μL, 14.97 μL, 20.00 μL, 24.77 μL, 29.20 μL, respectively, under the aforementioned conditions. Therefore the accuracies for the desired volumes were calculated as 5.33%, 0.22%, 0.00%, 0.93%, and 2.67%, which consistently outperformed that of the commercial pipettes (with a claimed accuracy of 5%). (Fan et al., 2018)

4.4.2 Optimization of washing, enzymatic reaction and antigen enrichment

In this part, we intended to optimize the key parameters in the Robotic ELISA workflow, such as finding the optimal washing cycles, the optimal duration of the enzymatic reaction, and the optimal pressure and cycles for antigen enrichment, to achieve a rapid yet reliable sample-to-answer scheme. (Zhao et al., 2020)

First, we investigated and determined the essential number of washing cycles for colorimetric readouts. One important criterion was that those HRP-CAP unbound to the antibodies (on the membrane) should be completely washed away to avoid interferences with the TMB-associated colorimetric reaction. Both membranes with or without the immobilized antibodies were prepared, and they were subsequently react-ed with HRP-CAP, followed by washing with PBS buffers for different washing cycles; finally, the colorimetric reagent of TMB substrate was added and the corresponding time-evolved colorimetric results were illustrated in Fig. 4-5a. As can be seen, for the control membrane without immobilized antibodies, its color turned from white to blue rapidly within 2 min without the washing step. With washing once, however, a small margin on the edge of the membrane turned blue after 10 min, indicating that the majority of the HRP-CAP had been washed away. As we further increased the washing cycles to 2 and 3, as shown in the third and fourth rows, the color of the membrane did not change, indicating that the washing cycles were adequate. We further confirmed these conclusions by designing a positive control test. A membrane with immobilized antibodies was prepared and reacted with HRP-CAP, and it was then washed twice and reacted with TMB substrates. The colorimetric readouts are shown in the last row of Fig 4-5a. As can be seen, the color of the membrane turned blue after 2 min of the enzymatic reaction. Overall, these results confirmed that the optimal washing cycle was 2 and therefore 2-cycle washing was used in all of the following experiments.

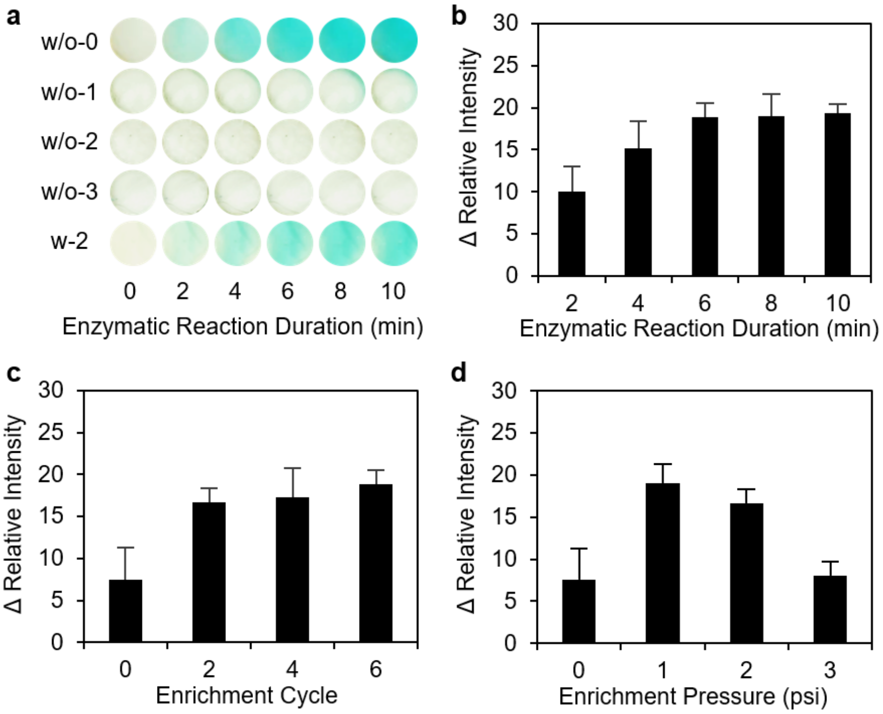

Fig. 4-5 Optimization of washing, enzymatic reaction, and antigen enrichment conditions. a) Images of the nanofibrous membrane with (w/) or without (w/o) the immobilized antibodies after adding the colorimetric reagent of TMB substrate to induce the enzymatic reaction under various washing cycles from 0 to 3. Comparison of the difference of the relative intensity value (i.e., ΔRI) under various b) enzymatic reaction durations from 2 to 10 min, c) enrichment cycles from 0 to 6, and d) pressure for enrichment flow from 0 to 3 psi ("0" means "no enrichment") between a negative control (PBS buffer) and a positive control (PBS buffer containing 1 ng/mL CAP). Note that the error bar indicates the measurement deviation between three different devices.

Next, we investigated the effects of the duration of enzymatic reaction on the colorimetric results, aiming to find the minimum incubation duration for reliable detection. Specifically, to quantify the color change of the nanofibrous membrane, the grayscale values (intensity) of the captured photos were extracted. (Liu et al., 2015; Luo et al., 2019) In particular, the averaged intensity value of each time-evolved photo was determined and the difference between the intensity value (at 2, 4, 6, 8 and 10 min) and the intensity value at the initial condition (0 min) was computed as Relative

Intensity (RI). Next, the RI difference (ΔRI) between the readouts from a positive control (1 ng/mL CAP) and a negative control (PBS buffer) was calculated and used as an indicator for the sensitivity of the detection: a larger ΔRI meant a greater sensitivity. As shown in Fig. 4-5b, ΔRI was 10.0 at 2 min, and it increased to 18.8 at 6 min and stayed almost still thereafter. Therefore, 6 min was considered the optimal duration for the enzymatic reaction and it was used in all of the subsequent experiments.

After that, we studied the enrichment conditions for the efficient Ag-Ab binding, including the enrichment cycle and the enrichment pressure, as summarized in Figs. 4-5c-d. Again, the ΔRI values between the control group of the PBS solution (negative) and the sample containing 1 ng/mL CAP (positive) were used to compare the colorimetric readouts. As shown in Fig. 4-5c, the ΔRI value was 7.5 without the enrichment cycle, and it increased to 16.7 after 2 cycles, 17.3 for 4 cycles and 18.8 for 6 cycles. As can be seen, the increase in the enrichment cycle had marginal effects on distinguishing the CAP-contained sample from the negative control. Consequently, 2-cycle enrichment was chosen as the optimal enrichment condition, which took approximately 200 s in total (1/3 that of the 6-cycle enrichment), to reduce the overall duration for the Robotic ELISA workflow. As can be seen, ΔRI for the 2-cycle enrichment was only less than 15% lower than that of the 6-cycle test. Though the sensitivity of detection was marginally compromised, the developed Robotic ELISA system was still capable of achieving a highly sensitive detection of our targeted analyte (CAP) in a short duration of mixing (within 2 cycles of enrichment).

Lastly, the effects of the enrichment pressure were also studied. As illustrated in Fig. 4-5d, the ΔRI value was 7.5 without the enrichment, and it increased to 19.0 at a pressure of 1 psi (with the flow rate of 0.41 μL/s); the ΔRI value decreased to 16.7 as the pressure increased to 2 psi (with the flow rate of 0.69 μL/s), and it dropped to 8.0 as we further increased the pressure to 3 psi (with the flow rate of 1.02 μL/s). Since higher enrichment pressure generated faster flow, the flow might be too rapid under a high pressure so that the duration left for the Ag-Ab binding was too short. (Sanjay et al., 2020) Although the ΔRI for the 2-psi enrichment was 11% lower than that of the 1-psi enrichment, the enrichment duration at 2 psi was half that of the enrichment duration at 1 psi. Therefore, to minimize the overall duration of the Robotic ELISA workflow, 2 psi was chosen as the optimal pressure for the enrichment flow.

4.4.3 Demonstration of the fully automated ELISA operations

As investigated in the previous Section, the optimized washing and reaction steps were applied, in which both the washing and enrichment cycles were 2 with the enzymatic reaction duration of 6 min under the enrichment pressure of 2 psi. To demonstrate the fully automated human-free sample-to-answer workflow, the Robotic ELISA platform was programmed for the detection of CAP concentration ranging from 0 to 2 ng/mL (or 0 to 6.2 nM) in PBS buffer (pH=7.4), which included the automated metering, mixing, washing and colorimetric readouts.

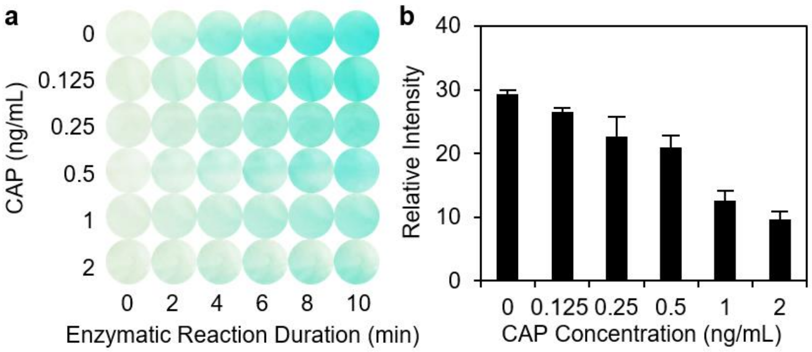

Fig. 4-6 a) Time-evolved optical images of the membrane from 0 to 10 min under various concentrations of CAP from 0 to 2 ng/mL, and b) Relative Intensity value between the colorimetric readouts at 6 min and the initial condition (0 min) under various concentrations of CAP from 0 to 2 ng/mL. Note that the error bar indicates the measurement deviation between three different devices.

Fig. 4-6a illustrates the time-evolution of the color change of the nanofibrous membrane during the enzymatic reaction, under six different CAP concentrations from 0 to 2 ng/mL. For each CAP concentration, a group of six photos was captured, which included the initial condition of the membrane and its subsequent conditions in every 2 min thereafter. As can be seen, for a low CAP concentration at 0 ng/mL, the color of the membrane was initially in light grey; the color started to change to blue after 2 min, and it rapidly turned into almost completely blue within 4 min and stayed almost unchanged afterwards. On the other hand, for the case of a high CAP concentration at 2 ng/mL, the initial col-or was the same with gradual transition to blue; however, the color change of the membrane was rather slow, and it stayed in the grey-blue mix even after 10 min of reaction. Such results confirmed the fact that the CAP from the sample competed with that in the HRP-CAP solution and there-fore it inhibited the binding of the HRP-CAP to the immobilized antibodies on the membrane, altering the colorimetric readouts.

Table 4-2 Selectivity of CAP detection for other common antibiotics at 1 ng/mL. Results are expressed in % relatively to responses between 0 and 1ng/mL CAP detection.

Antibiotic	**Florfenicol**	**Thiamphenicol**	**Penicillin**
Relative %	8.15%	2.79%	-0.75%

To further quantify the colorimetric results and determine the sensitivity and limit of detection (LOD), three devices were tested for each CAP concentration, and Fig. 4-6b showed the averaged results of the RI values. The linear range was found to be between 0 to 1 ng/mL (R2 =0.973). (Zhao et al., 2020) As can be seen, the RI value was 29.3 ± 0.58 for the CAP concentration of 0 ng/mL and it decreased to 12.7 ± 1.53 at 1 ng/mL. The absolute value of the sensitivity was therefore determined as 16.6/(ng/mL). Since the standard deviation of the negative control group was 0.58, the LOD was set at 0.1 ng/mL by its definition. (Long and Winefordner, 1983) The current LOD is well below the minimum required performance level for CAP in the United States (0.3 ng/mL). (Zhao et al., 2020) It is also worth noting that the LOD achieved by the Robotic ELISA system outperforms that conducted by manually operated nanofibrous membrane-based ELISA using the same colorimetric readout, which is 0.3 ng/mL. (Zhao et al., 2020) Furthermore, the LOD is comparable to the conventional microtiter plate reader-based ELISA detection. (Wesongah et al., 2007)

Table 4-3 Recovery of CAP from spiked salmon samples determined by the Robotic ELISA

Sample	**Spiked concentration (ng/mL)**	**Found concentration (ng/mL)**	**Recovery (%)**	**RSD (%)**
1	0	ND	-	0.57%
2	0.25	0.28	113.4%	6.53%
3	0.5	0.55	110.6%	9.93%
4	1.0	0.90	90.1%	9.25%

The selectivity of the developed Robotic ELISA system was tested by determining the response to three additional antibiotics in terms of CAP-equivalent concentration of 1 ng/mL expressed as a percentage of CAP response, including florfenicol (FF), thiamphenicol (TAP) and penicillin (PCN). As summarized in Table 4-2, the developed immunosensor showed a high specificity to CAP, since the results of the other antibiotics are all below LOD. To verify the feasibility of the Robotic ELISA for biological sample tests, three hybrid devices were prepared for the detection of salmon samples spiked with 0, 0.25, 0.5 and 1 ng/mL CAP. As shown Table 4-3, the respective recovery rates were not detectable (ND), 113.4%, 110.6% and 90.1% for each of the four concentrations. The relative standard deviations (RSDs) were from 0.57% to 9.93%. As a conclusion, these results demonstrate that the Robotic ELISA system can be successfully applied to the competitive ELISA in general with a low detection limit (of 0.1 ng/mL) in a fully automated and highly efficient fashion.

4.4 Conclusions

In summary, we have developed a fully automated platform, known as Robotic ELISA, seamlessly incorporating a robotic-microfluidic interface (RoMI) and a nanofibrous membrane-embedded hybrid microfluidic chip, for the human-free sample-to-answer workflow of the conventional ELISA tests. The Robotic ELISA allows automated multiplex operations such as high-precision pipetting, back-and-forth mixing and enrichment, washing and vision-unit enabled colorimetric readout. Compared to the existing ELISA automation solutions, the Robotic ELISA proposed here offers several distinct advantages: 1) fully automated ELISA detection; 2) short overall operation time (less than 20 min) from sample to answer; 3) high sensitivity and low limit of detection (0.1 ng/mL) in the detection of chloramphenicol; 4) low sample consumption (15 μL). However, the dynamic range of the NFM-based colorimetric ELISA detection is rather small, due to the limited color variations. To overcome this limitation, we could further design a multiplexed microfluidic chip with a set of colorimetric sensors targeting at different dynamic ranges; thereby expanding the detection range. It is worth-noting that the CAP ELISA assay only serves as a proof-of-concept demonstration of our methodology. Benefiting from its modular microfluidic design and seamless microfluidic-robotic interface, the proposed platform could be flexibly adapted to various robotic platforms and can be further configured to automate a broad range of biological operations in a simply programmable manner.

References

de Gennes, P.-G., Brochard-Wyart, F., Quéré, D., 2004. Capillarity and Wetting Phenomena, Capillarity and Wetting Phenomena. https://doi.org/10.1007/978-0-387-21656-0

Desmarchelier, A., Fan, K., Minh Tien, M., Savoy, M.C., Tarres, A., Fuger, D., Goyon, A., Bessaire, T., Mottier, P., 2018. Determination of 105 antibiotic, anti-inflammatory, antiparasitic agents and tranquilizers by LC-MS/MS based on an acidic QuEChERS-like extraction. Food Addit. Contam. - Part A Chem. Anal. Control. Expo. Risk Assess. 35. https://doi.org/10.1080/19440049.2018.1429677

Fan, J., Men, Y., Hao Tseng, K., Ding, Yi, Ding, Yunfeng, Villarreal, F., Tan, C., Li, B., Pan, T., 2018. Dotette: Programmable, high-precision, plug-and-play droplet pipetting. Biomicrofluidics 12. https://doi.org/10.1063/1.5030629

Liu, W., Guo, Y., Zhao, M., Li, H., Zhang, Z., 2015. Ring-Oven Washing Technique Integrated Paper-based Immunodevice for Sensitive Detection of Cancer Biomarker. Anal. Chem. 87, 7951–7957. https://doi.org/10.1021/acs.analchem.5b01814

Long, G.L., Winefordner, J.D., 1983. Limit of Detection: A Closer Look at the IUPAC Definition. Anal. Chem. 55, 712A-724A. https://doi.org/10.1021/ac00258a001

Luo, X., Xia, J., Jiang, X., Yang, M., Liu, S., 2019. Cellulose-Based Strips Designed Based on a Sensitive Enzyme Colorimetric Assay for the Low Concentration of Glucose Detection. Anal. Chem. 91, 15461–15468. https://doi.org/10.1021/acs.analchem.9b03180

Oh, K.W., Lee, K., Ahn, B., Furlani, E.P., 2012. Design of pressure-driven microfluidic networks using electric circuit analogy. Lab Chip. https://doi.org/10.1039/c2lc20799k

Sanjay, S.T., Li, M., Zhou, W., Li, Xiaochun, Li, XiuJun, 2020. A reusable PMMA/paper hybrid plug-and-play microfluidic device for an ultrasensitive immunoassay with a wide dynamic range. Microsystems Nanoeng. 6, 28. https://doi.org/10.1038/s41378-020-0143-5

Schindelin, J., Arganda-Carreras, I., Frise, E., Kaynig, V., Longair, M., Pietzsch, T., Preibisch, S., Rueden, C., Saalfeld, S., Schmid, B., Tinevez, J.Y., White, D.J., Hartenstein, V., Eliceiri, K., Tomancak, P., Cardona, A., 2012. Fiji: An open-source platform for biological-image analysis. Nat. Methods. https://doi.org/10.1038/nmeth.2019

Sutera, S.P., Skalak, R., 1993. The History of Poiseuille's Law. Annu. Rev. Fluid Mech. 25, 1–20. https://doi.org/10.1146/annurev.fl.25.010193.000245

Wang, J., Deng, K., Zhou, C., Fang, Z., Meyer, C., Deshpande, K.U.A., Li, Z., Mi, X., Luo, Q., Hammock, B.D., Tan, C., Chen, Y., Pan, T., 2019. Microfluidic cap-To-dispense (μCD): A universal microfluidic-robotic interface for automated pipette-free high-precision liquid handling. Lab Chip 19, 3405–3415. https://doi.org/10.1039/c9lc00622b

Wesongah, J.O., Murilla, G.A., Guantai, A.N., Elliot, C., Fodey, T., Cannavan, A., 2007. A competitive enzyme-linked immunosorbent assay for determination of chloramphenicol. J. Vet. Pharmacol. Ther. 30, 68–73.

Zhao, C., Si, Y., Pan, B., Taha, A.Y., Pan, T., Sun, G., 2020. Design and fabrication of a highly sensitive and naked-eye distinguishable colorimetric biosensor for chloramphenicol detection by using ELISA on nanofibrous membranes. Talanta 217. https://doi.org/10.1016/j.talanta.2020.121054

Chapter 5 Conclusion and Future Directions

5.1 Summary

This dissertation focuses on the design and development of a universal robotic-microfluidic interface (RoMI), as well as examples of modular microfluidics for automated, accurate and efficient biochemical analyses. The entire work was initiated with the novel idea of automating different microfluidic modules by sharing seamless and reversible connectors between the robotic end-effectors and the microfluidic inlets. First, we have designed and fabricated a pair of RoMI connectors and microfluidic printing modules, that can fully automate high precision and low-volume liquid handling operations. Next, we have developed a novel two-step strategy for combinatorial studies of protein networks. The developed strategy featured at minimizing hands-on operations by using the RoMI system for low-volume liquid handling; eliminating cross-contamination by using low-cost and disposable microfluidic printing modules; mimicking the cell environment by forming water-in-oil droplets surrounded by a lipid membrane; and comparing free/immobilized kinases activities by introducing protein-lipid bindings. These features make RoMI a promising tool for *in vitro* protein network studies. Lastly, we have presented a system that incorporates a RoMI and a hybrid microfluidic module, which embeds a highly sensitive nanofibrous membrane for fully automated ELISA tests. This system could automate a series of liquid-handling operations in a typical ELISA protocol, including pipetting, mixing and washing. In addition, a vision unit has been integrated on the robotic arms to perform colorimetric measurement, thereby realizing sample-to-answer ELISA analysis. Overall, the RoMI system have several advantages compared with traditional microfluidic systems: 1) employing robotics to automate microfluidics; 2) replacing complex integrated microfluidic design with simplest module design; 3) making full use of external infrastructure settings (e.g., pumps, valves, pressure regulators); 4) establishing an open-source platform accessible to all biochemical communities. RoMI provides insights into how to transform microfluidic technologies into powerful tools in future laboratory automation.

5.2 Prospective Directions

5.2.1 Microfluidic module for advanced biomedical analyses

The traditional microfluidic platform has invested considerable efforts in integrating microfluidic units and the corresponding control devices together to achieve the automation of a specific laboratory protocol. (Haeberle and Zengerle, 2007; Nahavandi et al., 2014) In this dissertation, we show the possibility of minimizing these efforts by using RoMI to process various microfluidic modules. As a next step, we can automate more laboratory operation units by designing more microfluidic modules, such as an extraction module that embeds a binding membrane and a separation module that is integrated with a liquid chromatography column. By expanding the types of microfluidics modules, RoMI can automate increasingly complex and laborious laboratory protocols.

RoMI can not only meet the needs of traditional laboratory automation, but can also automate the latest microfluidic-based devices. For instance, droplet digital polymerase chain reaction (ddPCR) has developed rapidly in the past decade, where a T-junction or a cross-junction is used to isolate bulk solution into discrete droplets that contain zero or one nucleic acid molecule. (Pekin et al., 2011) RoMI can be adapted to handle these droplet generation modules and potentially automate ddPCR detections. In addition, single-cell detection is becoming more attractive in biomedical research and clinical diagnosis, which allows a better understanding of cellular heterogeneity and possibly new diagnostic and therapeutic approaches. (Luo et al., 2019; Shinde et al., 2018)

Recently, a number of microfluidic devices have been developed for single-cell encapsulation (Alkayyali et al., 2019), single-cell sorting (Sajeesh and Sen, 2014; Wyatt Shields Iv et al., 2015) and even on-chip single-cell detection (Gao et al., 2019; Murphy et al., 2018). RoMI can also involve more microfluidic modules for single-cell studies.

5.2.2 RoMI for future laboratory automation

With the rapid development of artificial intelligence and machine learning, laboratory robots are not only responsible for hands-on operations, but can also plan experiments, analyze data and even make decisions. Recently, a variety of laboratory robots have been developed that can walk around in a laboratory and operate laboratory instruments. (Biermann et al., 2021; Holland and Davies, 2020) However, it would be a better choice for RoMI to integrate the most advanced small-sized sensing modules (e.g., optical, electronic, electrochemical, electromagnetic) instead of handling bulky detection instruments. Moreover, extra robotic arms can be introduced in RoMI so that multiple modules (both microfluidic and sensing modules) can work in a collaborative manner. In addition, RoMI would benefit from the use of more algorithms to analyze various types of data, as well as logical judgments for experiment design. For instance, RoMI would be a promising robot for drug screening, where it could cyclically perform high-throughput screening to select/exclude candidates. As collaborative and interdisciplinary research becomes increasingly dominant, we hope RoMI can serve as an example for bringing the most advanced engineering technologies to advanced biomedical studies.

References

Alkayyali, T., Cameron, T., Haltli, B., Kerr, R.G., Ahmadi, A., 2019. Microfluidic and cross-linking methods for encapsulation of living cells and bacteria - A review. Anal. Chim. Acta. https://doi.org/10.1016/j.aca.2018.12.056

Biermann, F., Mathews, J., Nießing, B., König, N., Schmitt, R.H., 2021. Automating laboratory processes by connecting biotech and robotic devices—an overview of the current challenges, existing solutions and ongoing developments. Processes 9. https://doi.org/10.3390/pr9060966

Gao, D., Jin, F., Zhou, M., Jiang, Y., 2019. Recent advances in single cell manipulation and biochemical analysis on microfluidics. Analyst. https://doi.org/10.1039/c8an01186a

Haeberle, S., Zengerle, R., 2007. Microfluidic platforms for lab-on-a-chip applications. Lab Chip. https://doi.org/10.1039/b706364b

Holland, I., Davies, J.A., 2020. Automation in the Life Science Research Laboratory. Front. Bioeng. Biotechnol. https://doi.org/10.3389/fbioe.2020.571777

Luo, T., Fan, L., Zhu, R., Sun, D., 2019. Microfluidic single-cell manipulation and analysis: Methods and applications. Micromachines. https://doi.org/10.3390/mi10020104

Murphy, T.W., Zhang, Q., Naler, L.B., Ma, S., Lu, C., 2018. Recent advances in the use of microfluidic technologies for single cell analysis. Analyst. https://doi.org/10.1039/c7an01346a

Nahavandi, Sofia, Baratchi, S., Soffe, R., Tang, S.Y., Nahavandi, Saeid, Mitchell, A., Khoshmanesh, K., 2014. Microfluidic platforms for biomarker analysis. Lab Chip. https://doi.org/10.1039/c3lc51124c

Pekin, D., Skhiri, Y., Baret, J.C., Le Corre, D., Mazutis, L., Ben Salem, C., Millot, F., El Harrak, A., Hutchison, J.B., Larson, J.W., Link, D.R., Laurent-Puig, P., Griffiths, A.D., Taly, V., 2011. Quantitative and sensitive detection of rare mutations using droplet-based microfluidics. Lab Chip. https://doi.org/10.1039/c1lc20128j

Sajeesh, P., Sen, A.K., 2014. Particle separation and sorting in microfluidic devices: A review. Microfluid. Nanofluidics. https://doi.org/10.1007/s10404-013-1291-9

Shinde, P., Mohan, L., Kumar, A., Dey, K., Maddi, A., Patananan, A.N., Tseng, F.G., Chang, H.Y., Nagai, M., Santra, T.S., 2018. Current trends of microfluidic single-cell technologies. Int. J. Mol. Sci. https://doi.org/10.3390/ijms19103143

Wyatt Shields Iv, C., Reyes, C.D., López, G.P., 2015. Microfluidic cell sorting: A review of the advances in the separation of cells from debulking to rare cell isolation. Lab Chip. https://doi.org/10.1039/c4lc01246a